The Astrophysical Journal, 977:136 (21pp), 2024 December 10 https://doi.org/10.3847/1538-4357/ad85e5

X-Ray Spectroscopy of the Dwarf Nova Z Chamaeleontis in Quiescence and Outburst Using the XMM-Newton Observatory

Şölen Balman[1,2], Eric M. Schlegel[3], Patrick Godon[4,5], and Jeremy J. Drake[6]
[1] Department of Astronomy and Space Sciences, Faculty of Science, Istanbul University, Beyazit, 34119, Istanbul, Türkiye; solen.balman@gmail.com, solen.balman@istanbul.edu.tr
[2] Kadir Has University, Faculty of Engineering and Natural Sciences, Cibali, 34083, Istanbul, Türkiye
[3] Department of Physics and Astronomy, University of Texas-San Antonio, San Antonio, TX 78249, USA
[4] Department of Astrophysics & Planetary Science, Villanova University, 800 Lancaster Ave., Villanova, PA 19085, USA
[5] Henry A. Rowland Department of Physics & Astronomy, Johns Hopkins University, Baltimore, MD 21218, USA
[6] Lockheed Martin Solar and Astrophysics Laboratory, 3251 Hanover St., Palo Alto, CA 94304, USA
Received 2024 August 19; revised 2024 October 7; accepted 2024 October 9; published 2024 December 9

Abstract

We present X-ray spectroscopy of the SU UMa–type dwarf nova Z Chamaeleontis using the European Photon Imaging Camera and reflection grating spectrometer (RGS) instruments on board the XMM-Newton observatory. The quiescent system can be modeled by collisional equilibrium (CIE) or nonequilibrium plasma models, yielding a kT of 8.2–13.0 keV at a luminosity of $(5.0–6.0)\times10^{30}$ erg s^{-1}. The spectra yield better χ^2_ν using partially covering absorbers of cold and/or photoionized nature. The ionized absorber has an equivalent $N_{\rm H}=(3.4–5.9)\times10^{22}$ cm^{-2} and a $\log(\xi)=3.5–3.7$ with a (50–60)% covering fraction when the VNEI model (XSPEC) is used. The line diagnosis in quiescence shows no resonance lines, with only the forbidden lines of Ne, Mg, and Si detected. The H-like C, O, Ne, and Mg are detected. The strongest line is O VIII, with $(2.7–4.6)\times10^{-14}$ erg s^{-1} cm^{-2}. The quiescent X-ray-emitting plasma is not collisional and not in ionization equilibrium, which is consistent with hot ADAF-like accretion flows. The line diagnosis in the outburst shows He-like O and Ne, with intercombination lines being the strongest, along with weaker resonance lines. This indicates the plasma is more collisional and denser, but not yet in CIE, revealing ionization timescales of $(0.97–1.4)\times10^{11}$ s cm^{-3}. The R ratios in the outburst yield electron densities of $(7–90)\times10^{11}$ cm^{-3} and the G ratios yield electron temperatures of $(2–3)\times10^{6}$ K. The outburst luminosity is $(1.4–2.5)\times10^{30}$ erg s^{-1}. The flow is inhomogeneous in density. All detected lines are narrow, with widths limited by the resolution of RGS, yielding Keplerian rotational velocities <1000 km s^{-1}. This is too low for boundary layers, consistent with the nature of ADAF-like hot flows.

Unified Astronomy Thesaurus concepts: Cataclysmic variable stars (203); Dwarf novae (418); Accretion (14); Stellar accretion disks (1579); Atomic spectroscopy (2099); Line intensities (2084); Space plasmas (1544); Astrophysical processes (104); Close binary stars (254); X-ray transient sources (1852)

1. Introduction

Cataclysmic variables (CVs) are close binary systems where a white dwarf (WD) accretes matter from a late-type Roche-lobe-filling main-sequence star (B. Warner 1995). In nonmagnetic (or weakly magnetic) CVs, an accretion disk is assumed to reach all the way to the WD surface. Dwarf novae (DNe) are a class of nonmagnetic CVs where ongoing accretion at a low rate (quiescence) is interrupted every few weeks to months or sometimes at longer durations by intense accretion (outburst) of days to weeks, where $\dot{M}$ increases (see Ş. Balman 2020; J. M. Hameury et al. 2020 for reviews). There are also a few magnetic CVs (i.e., intermediate polars) that show DN-type outbursts. Standard accretion-disk (SAD) theory (N. I. Shakura & R. A. Sunyaev 1973) predicts half of the accretion luminosity to emerge from the disk and the other half from the boundary layer (BL) very close to the WD (D. Lynden-Bell & J. E. Pringle 1974). The theoretically expected BL emission is such that during low-mass accretion states ($\dot{M}_{\rm acc}<10^{-(9-9.5)}\,M_\odot$), it is optically thin in the hard X-rays (R. Narayan & R. Popham 1993; R. Popham 1999), and for high-accretion-rate states ($\dot{M}_{\rm acc}>10^{-(9-9.5)}\,M_\odot$), it is optically thick in the soft X-rays and EUV; $kT\sim10^{5-5.6}$ K (P. Godon et al. 1995; R. Popham & R. Narayan 1995; M. Hertfelder & W. Kley 2015, 2017). It has been shown that the optically thin BLs can be radially extended, advecting part of the energy to the WD as a result of their inability to cool (R. Narayan & R. Popham 1993). The SAD is often found inadequate for modeling high-state CVs (nova-likes; NLs), as well as some eclipsing quiescent DNe in the UV and/or optical, generating a spectrum that is bluer than the observed UV spectra, indicating that a hot optically thick inner disk is considerably colder than predicted by theory (R. E. Puebla et al. 2007; A. P. Linnell et al. 2010). As a result, recent SAD models have used a truncated inner-optically-thick disk (see P. Godon et al. 2017) that models the UV data adequately. Moreover, the Balmer jump (absorption due to H Balmer series) is missing in CVs (C. La Dous 1989; C. Knigge et al. 1998). These observations in the UV and the optical indicate that the radial temperature profile in SAD flows needs to be modified, decreasing it in the inner disk and increasing it in the outer disk. A recent model alternative to the basic SAD flow has used large magnetically controlled zones that transfer mass and angular momentum outward, which flattens the spectral continuum in the optical and UV to produce this observed effect (C. J. Nixon & J. E. Pringle 2019). A more recent model (I. Hubeny & K. S. Long 2021) produces similar effects by changing the temperature structure in the SAD, where a vertical

temperature structure is not maintained and most of the dissipation occurs from the heated surface layers (instead of midplane, as in an SAD flow) without a need for inner truncation. However, these models cannot accommodate and explain the extent and/or emission characteristics of the X-ray region (e.g., hard X-rays). The accretion flows in high-state CVs, NLs, and DNe are well explained in the context of radiatively inefficient advective hot flows as opposed to standard optically thick accretion flows, which form in the inner disk, explaining most of the complexities in the X-rays and other wavelengths (Ş. Balman 2020; Ş. Balman et al. 2022). Shock formation in advection-dominated accretion flows (ADAFs) around accreting WDs has been calculated (S. R. Datta et al. 2021) and a shock occurs around 1.3×10^9 cm from the WD surface (about 1.5–2.5 R_{wd}, depending on the WD mass), which may explain the hard-X-ray emission.

1.1. X-Ray Characteristics of DNe

One of the earliest comprehensive studies on the X-ray emission of accreting nonmagnetic CVs using the EINSTEIN IPC (0.2–4 keV) showed that they mostly emit hard-X-ray emission in this range, with luminosities $\leqslant$a few $\times$ 10^{32} erg s^{-1}(J. Patterson & J. C. Raymond 1985). The DNe in quiescence (low-$\dot{M}$ systems) were observed with subsequent X-ray telescopes (e.g., RXTE, XMM-Newton, Chandra, Suzaku, Swift, NuSTAR, and NICER) and the results seem in accordance with one-dimensional numerical simulations of the optically thin BLs in standard steady-state disks in quiescence with low accretion rates (e.g., P. Szkody et al. 2002; D. Pandel et al. 2005; V. R. Rana et al. 2006; M. Ishida et al. 2009; Ş. Balman et al. 2011; A. A. Nucita et al. 2011; Q. Wada et al. 2017; A. Dobrotka et al. 2023; A. Dutta et al. 2023; M. Kimura et al. 2023).

On the other hand, studies of the X-ray variability and inner disk structure of DNe in quiescence (and outburst) reveal optically thick disk truncation and the plausible formation of hot (coronal) flows in the inner parts of the quiescent DN accretion disks (Ş. Balman & M. Revnivtsev 2012; A. Dobrotka et al. 2016, 2023; Ş. Balman 2019, 2020). Moreover, the optically thick disk truncation, as in X-ray binaries, is supported with simulations and light-curve modeling of some DNe (J. M. Hameury & J. P. Lasota 2021). The aperiodic timing variability is used to derive broadband noise power spectra, where the break frequencies in the characteristic power-law red-noise structure show the change in and the diminishing Keplerian flow of a standard Keplerian disk into a sub-Keplerian advective hot flow. The range of break frequencies is 1–6 mHz for quiescent DNe, translating to a transition radius of $(3–10) \times 10^9$ cm (Ş. Balman & M. Revnivtsev 2012; Ş. Balman 2020). Detailed cross-correlation analyses of DN light curves show 90–180 minutes lags of X-rays with respect to UV, indicating propagation delays and the change of flow structure (Ş. Balman & M. Revnivtsev 2012) into advective hot flows within DN disks. SS Cyg shows 0.26–3.11 s optical lags (X-rays), indicating X-ray reprocessing and irradiation in the disk (Y. Nishino et al. 2022). E. Aranzana et al. (2018) find 5 s soft lags in the optical (red lags the blue), revealing reprocessing and thermal timescale effects.

The optically thin hard-X-ray emission with virial temperatures in the X-ray-emitting region plus the lack of soft-X-ray emission at high states have been interpreted as the existence of ADAF-like radiatively inefficient advective accretion flows near the WD (Ş. Balman 2020; M. Kimura et al. 2021; Ş. Balman et al. 2022 and references therein). From an analysis of Kepler data of MV Lyr (an NL; high-state CV), it was proposed that in the very inner region (e.g., BL), the geometrically thin, optically thick disk is surrounded by a geometrically thick and optically thin disk—the sandwich model (S. Scaringi 2014). This sandwich model may explain the connection between X-rays and optical together with the detection of the same frequency (flickering) in both bands in other DN systems (A. Dobrotka et al. 2023 and references therein).

DN outbursts are brightenings of the accretion disks as a result of thermal viscous instabilities summarized in the disk instability model (DIM; J.-P. Lasota 2001, 2004, 2008; J. M. Hameury et al. 2020). Other supporting calculations are the tidal thermal instability in DN outbursts (Y. Osaki 1996) and enhanced mass transfer aiding the outbursts (J.-M. Hameury et al. 2000). During the outburst stage, the X-ray spectra of DNe differ from quiescence, since the accretion rates are higher (10^{-10}–10^{-8} $M_\odot$ yr^{-1}; C. Knigge et al. 2011) and the BL is expected to be optically thick, emitting EUV/soft X-rays (see the X-ray reviews in E. Kuulkers et al. 2006; K. Mukai 2017). Such soft-X-ray/EUV components with temperatures in a range 5–30 eV are detected only from about six systems as compared to all DNe (e.g., C. W. Mauche et al. 1995; K. S. Long et al. 1996; C. W. Mauche & J. C. Raymond 2000; C. W. Mauche 2004; K. Byckling et al. 2009; M. Kimura et al. 2023). On the other hand, as a more frequently detected emission component (all DNe), DNe show hard-X-ray emission during the outburst stage at lower flux levels and X-ray temperature compared with quiescence (e.g., P. J. Wheatley et al. 2003; K. E. McGowan et al. 2004; M. Ishida et al. 2009; D. J. Collins & P. J. Wheatley 2010; D. Fertig et al. 2011; Ş. Balman 2015; A. Dobrotka et al. 2023; A. Dutta et al. 2023). Few DNe show increased levels of hard-X-ray emission (GW Lib and U Gem: T. Güver et al. 2006; K. Byckling et al. 2009; M. Takeo et al. 2021). The total X-ray luminosity during outburst is 10^{30}–10^{34} erg s^{-1}, where the upper level is observed when the soft component is detected. Grating spectroscopy of the outburst data (SS Cyg and U Gem) indicates large widths for lines with velocities in excess of 1000 km s^{-1}, mostly of H and He-like emission lines (C, N, O, Ne, Mg, Si, Fe, etc.; C. W. Mauche 2004; V. R. Rana et al. 2006; S. Okada et al. 2008). A characteristic of some DN outburst light curves is the UV and X-ray delays of several hours up to 2 days, in the rise to outburst (with respect to optical), indicating possible disk truncation (F. Meyer & E. Meyer-Hofmeister 1994; R. Stehle & A. R. King 1999; M. R. Schreiber et al. 2003). During outburst, no X-ray eclipses are detected in the eclipsing systems (particularly of soft-X-ray emission) or no distinct orbital variations are seen (e.g., G. W. Pratt et al. 1999; K. Byckling et al. 2009).

1.2. Z Chamaeleontis

Z Chamaeleontis (Z Cha) is a DN of the SU UMa subclass, showing normal and superoutbursts (F. M. Bateson 1978; J. Smak 1979). The importance of Z Cha among the DNe lies in the complexity of its eclipse structure, which is a superposition of total eclipses of both the WD and the hotspot (B. Warner 1974; J. Bailey 1979). Other similar DNe are OY Car, HT Cas, and V2051 Oph (J. H. Wood & K. Horne 1990). The detailed eclipse structure reveals the system parameters. The binary is highly inclined with $i = 81.^\circ6$–$81.^\circ9$ (J. Wood et al. 1986;

J. Smak 2007), thus deep eclipses affect the optical light curves. Z Cha has an orbital period of 1.78 hr with a WD mass of 0.54–0.84 $M_{\odot}$ and a secondary mass of 0.081 $M_{\odot}$, with a ratio of secondary to primary mass $q = 0.2$ (J. Wood et al. 1986; R. A. Wade & K. Horne 1988; R. Baptista et al. 2002; J. Smak 2007). A distance of 97 pc has been long accepted for Z Cha (J. Wood et al. 1986). The GAIA archive[7] yields a distance of 120 ± 33 pc using the parallax measurement, which is in agreement with the accepted value. The X-ray properties observed with ROSAT PSPC are a temperature $kT =$ 2.6–19 keV and an $N_{\rm H} = (1.3\text{–}2.3) \times 10^{20}\,{\rm cm}^{-2}$, translating to a luminosity of $2.5 \times 10^{30}\,{\rm erg\,s}^{-1}$ (bolometric) at an accretion rate of $\sim 10^{-12}\,M_{\odot}\,{\rm yr}^{-1}$ (see A. van Teeseling 1997). The quiescent-phase XMM-Newton data of Z Cha have been previously presented in A. A. Nucita et al. (2011) and are reanalyzed in this paper, and the differences in results will be discussed in the analysis and results sections. The archival XMM-Newton data of Z Cha in the outburst stage are analyzed for the first time and discussed in this paper.

2. The Observations and Data

The XMM-Newton observatory (F. Jansen et al. 2001) has three 1500 $\rm cm^2$ X-ray telescopes, each equipped with a European Photon Imaging Camera (EPIC) at the focus, where two of them have metal oxide semiconductor (MOS) CCDs (M. J. L. Turner et al. 2001) and the last one uses pn CCDs (L. Strüder et al. 2001) for data recording. About half the X-rays are diverted, by reflection grating arrays, to the reflection grating spectrometers (RGSs; J. W. den Herder et al. 2001), which provide high-resolution ($\lambda/\Delta\lambda \sim$ 100–800) X-ray spectroscopy in the 0.33–2.5 keV range. The EPIC cameras acquire data in the 0.1–15 keV range, with a field of view of $\sim 30'$ diameter. The optical monitor (OM), a photon-counting instrument, is a coaligned 30 cm optical/UV telescope, providing a possibility of observing simultaneously in the X-ray and optical/UV wavelengths (K. O. Mason et al. 2001), with an imaging capability in three broadband UV filters and three optical filters spanning 1800–6000 Å.

Z Cha was observed (pointed observation) by XMM-Newton on two different occasions: in quiescence (OBS ID = 0205770101) and in outburst (OBS ID = 0306560301). The pointed observation during quiescence was obtained between 2003 December 19 UT 20:46:36 and 2003 December 21 UT 00:52:53, with a duration of ~100 ks. A thin optical blocking filter was used with all the EPIC cameras. The pn instrument was operated in the full-frame imaging mode. The MOS1 and MOS2 CCDs were used in the large-window imaging mode. Z Cha was detected with a count rate of $1.1 \pm 0.004\,{\rm c\,s}^{-1}$, $0.36 \pm 0.002\,{\rm c\,s}^{-1}$, and $0.34 \pm 0.002\,{\rm c\,s}^{-1}$ using the EPIC pn, MOS1, and MOS2 instruments, respectively. The combined RGS (1+2) spectrum has a count rate of $0.024 \pm 0.0006\,{\rm c\,s}^{-1}$. The pointed observation during outburst was obtained between 2005 September 30 UT 01:45:43 and 2005 October 01 UT 01:56:20, with a duration of ~90 ks. A medium optical blocking filter was used with all the EPIC cameras, where the pn data were obtained in the full-frame imaging mode and the MOS CCDs were operated with the large-window imaging mode. Z Cha was detected with a count rate of $0.31 \pm 0.002\,{\rm c\,s}^{-1}$, $0.081 \pm 0.001\,{\rm c\,s}^{-1}$, and $0.076 \pm 0.001\,{\rm c\,s}^{-1}$ using the EPIC pn, MOS1, and MOS2 instruments, respectively. The combined RGS (1+2) spectrum has a count rate of $0.0093 \pm 0.0006\,{\rm c\,s}^{-1}$.

We analyzed the pipeline-processed data using Science Analysis Software (SAS) version 17.0.0-21.0.0. The pipeline-processed events were also checked using the SAS tasks *epproc* and *emproc* to make sure there are no differences relating to software or processing versions. The RGS spectra and response files were created with the SAS task *rgsproc*. Data (single- and double-pixel events; i.e., patterns 0–4 with the Flag=0 option for pn and patterns ⩽12 for MOS) were extracted from a circular region of radius 35″–40″ for pn, MOS1, and MOS2 in order to perform spectral analysis. The background events were extracted from a source-free zone close to the source and normalized to the same extraction area. The EPIC spectra were created using the task *especget*. The RGS spectra were created with the *rgsproc* task and coadded utilizing the SAS task *rgscombine*. The *especget* and *rgsproc* tasks also create the necessary response and ancillary files for the analysis. The task descriptions and documentations are available online at the ESA website.[8]

For our timing analysis purposes, we utilized the data collected with the EPIC cameras in the large-window imaging mode, separately, using the pn and MOS 1 and 2, and the OM data using the fast-imaging mode (⩾0.5 s time resolution) with the B filter (3980–4334 Å). The time resolution of the imaging modes of the pn CCDs is 70 ms, which is more than adequate for our timing analysis. We checked/cleaned the pipeline-processed/produced event files from existing flaring episodes for both of the Z Cha observations. The OM data were analyzed using *omfchain* with 0.5 s time resolution (bin time). EPIC light curves were created with the task *evselect*. Identical region files used in the spectral analysis were used to extract source and background light curves. Further reductions and analyses of spectra and light curves were performed using HEASoft[9] (version 6.24–6.32), using the XRONOS or XSPEC software within the HEASoft distributions.

3. Temporal Analysis and Optical Eclipse Times in the X-Ray Data

We extracted light curves from the quiescent and outburst XMM-Newton EPIC data sets between 0.2 and 10 keV using the SAS task *evselect* at 0.01 s resolution for quiescence and outburst. Circular regions with a range of radius 35″–40″ were used for the photon extraction to calculate both the source and the background light curves (devoid of other contaminating sources). Finally, background-subtracted light curves were attained using the XRONOS task *lcmath*. Barycentric correction was applied on both of the event files (outburst and quiescence). Next, we folded the EPIC pn, MOS1, and MOS2 light curves in outburst and quiescence over the orbital period using the ephemerides by R. Baptista et al. (2002); $T_0 =$ (BJD)2440264.68070(±4) + 0.0744993048 (±5) × E days. We note here that A. A. Nucita et al. (2011) present a quiescent optical B-band light-curve analysis for Z Cha in detail together with the eclipses and the EPIC temporal analysis (quiescence), which we omit here.

M. C. Cook & B. Warner (1984) have performed a detailed analysis of the optical band eclipses of Z Cha and found that the WD eclipse is around phases 0.97–1.03 and the hotspot

[7] https://gea.esac.esa.int/archive

[8] http://xmm2.esac.esa.int/sas/

[9] https://heasarc.gsfc.nasa.gov/docs/software/heasoft/

eclipse is around 0.99–1.1. We underline that the occultation of the accretion impact zone and the occultation of the WD overlap closely in phase for Z Cha, which means that the accretion impact zone is in the line of sight toward the WD at the times of the eclipses. A. A. Nucita et al. (2011) find an average EPIC rate of $0.7 \pm 0.1\,\mathrm{c\,s^{-1}}$ and a rate of $0.033 \pm 0.003\,\mathrm{c\,s^{-1}}$ during the eclipses in quiescence. They calculate that the X-ray ingress and egress are about 40 and 54 s, respectively, with an eclipse duration (mid-ingress to mid-egress) of 324 ± 9 s. However, the analysis of several consecutive eclipses with the ROSAT HRI (0.2–2.4 keV) yielded eclipse durations of 350–520 s (during quiescence) which are longer than XMM-Newton (A. van Teeseling 1997). Our re-analysis of the EPIC pn light curve for the source rate during the inferred eclipse times by A. A. Nucita et al. (2011) reveals that in most cases the source is not detected with only a few photons in the given time interval. Figure 1 shows the quiescent EPIC pn light curve with a high time resolution of 1 s, at the times of the eclipses. This bin time is particularly chosen so that given the $1.1\,\mathrm{c\,s^{-1}}$ EPIC pn count rate, there is one photon per bin in the figure. We find that the eclipse times contain variable numbers of X-ray photons around 4–13 (except for the very beginning and end of the eclipse durations, which are likely associated with the ingress and egress). An inspection of the 13 optical eclipses in the *B*-band light curve (XMM-Newton OM in quiescence) yields 280–300 s eclipse durations, assuming a width of the time interval at the half of the brightness that is out of eclipse on the egress side. We see that the X-ray source is not detected at all during these times. As a result, we take it that the disappearance of the source for a short time interval, given the low count rate of Z Cha, may result from occultation of the X-ray emission region and/or from any absorbers that reside on the disk or the accretion impact zone (given the high inclination). We will elaborate on this in our results and the discussion sections. Therefore, we do not exclude eclipse times from spectral analysis, since the source is not detected in the X-rays during these times (see Figure 1).

The upper left panel of Figure 2 presents the optical *B*-band light curve binned at 10 s, which shows deep variations at the eclipse times (no full eclipses) during the outburst observation. The upper right panel displays the mean *B*-band light curve folded at the orbital period with the ephemerides given in the first paragraph of this section. The lower left panel shows the EPIC light curve (a 250 s bin time is used) obtained during the outburst, and the lower right panel displays the folded EPIC light curve at the orbital period using 15 phase bins (during the outburst). We find a weak orbital variation with a modulation depth of 13% ($[\max - \min/\max + \min] \times 100$). The modulation depth for the *B*-band data is about 32% using the mean light curve. However, this value changes between 43% and 28% in the *B*-band light curve. We note that the combined EPIC light curve was attained using background-subtracted pn and MOS1 and MOS2 light curves. We have checked to see if any asynchronicity affected our folding procedure. The individual instrument light curves are slightly different, but our folded EPIC light curve resembles the EPIC pn light curve very closely, as expected, since the pn has higher sensitivity (a rate of three to four times more) compared with MOS1 and MOS2. The timing analyses (for quiescence) using power-density spectra for the broadband noise analysis, the derivation of the break frequency, and the cross-correlation analysis are presented in Ş. Balman (2020), which we elaborate in the discussion section.

4. Spectral Analysis and Results

4.1. Analysis of EPIC Data in Quiescence

The background and source spectra, response files, and ancillary files were generated for Z Cha as described in Section 2. The EPIC spectra were grouped with minimum counts of 90, 65, and 70 in each spectral bin for pn, MOS1, and MOS2, respectively, to acquire good χ^2 statistics. The spectral analysis is performed via simultaneous/joint analysis of all three spectra within the XSPEC software (for references and model descriptions, see K. A. Arnaud 1996).[10] During the entire spectral analysis, constant multiplicative models (multiplicative constants) have been incorporated in the fits, to account for the cross-normalization calibration between spectra from the different detectors on board XMM-Newton. To account for the interstellar and/or intrinsic absorption in the broadband X-ray spectra, the *tbabs* model (J. Wilms et al. 2000) was utilized in the fitting procedures (abundances set to abund=wilm; J. Wilms et al. 2000). However, we used other absorption models in the fitting procedure, *pcfabs* and *zxipcf*, which are partially covering cold and ionized absorber models, respectively, which yielded better fits when used along with the plasma models. The joint X-ray spectra (pn, MOS1, and MOS2) are fit with the multitemperature isobaric cooling flow type of plasma emission model CEVMKL in XSPEC (D. A. Liedahl et al. 1995; K. P. Singh et al. 1996), with switch=2, where the CEVMKL interpolates using the APEC model and ATOMDB[11] database. For comparison and to understand the nature of the flow, we also utilized the VNEI[12] model (a nonequilibrium ionization plasma model in XSPEC), which uses the NEIvers.3.0.9 plasma code with the ATOMDB database.

Quiescent DNe show several H- and He-like emission lines from the elements N to Fe, and some Fe L-shell lines, revealing the existence of hot, optically thin, X-ray-emitting plasma in these systems (see the reviews of Ş. Balman 2012; Ş. Balman 2020), as the accreting material settles onto the WD. This region is found to form a structure with a continuous temperature distribution in the X-rays (as in a cooling flow plasma). The emission measure at each temperature is proportional to the time the cooling gas remains at this temperature. This emission represents a collisionally ionized plasma in thermal equilibrium between electrons and ions.

As a first step, we have fitted the quiescent EPIC pn and MOS1–2 spectra simultaneously with the simple model (*tbabs* × CEVMKL), and the α parameter that describes the index of the temperature distribution for the CEVMKL model was set free, since a χ^2_ν value below 2.0 (i.e., an acceptable fit) could not be achieved otherwise. The spectral parameters are given in the QFit-1 column of Table 1, and all the other fit results (QFit-1 to QFit-6) are tabulated there as well. The spectrum fit with this model is displayed in Figure 3, along with some other example fit spectra from the sample QFit-1 to QFit-6. The range of neutral hydrogen column densities derived from QFit-1 is checked using standard tools that

[10] https://heasarc.gsfc.nasa.gov/xanadu/xspec/manual/Models.html
[11] http://atomdb.org
[12] https://heasarc.gsfc.nasa.gov/xanadu/xspec/manual/node195.html

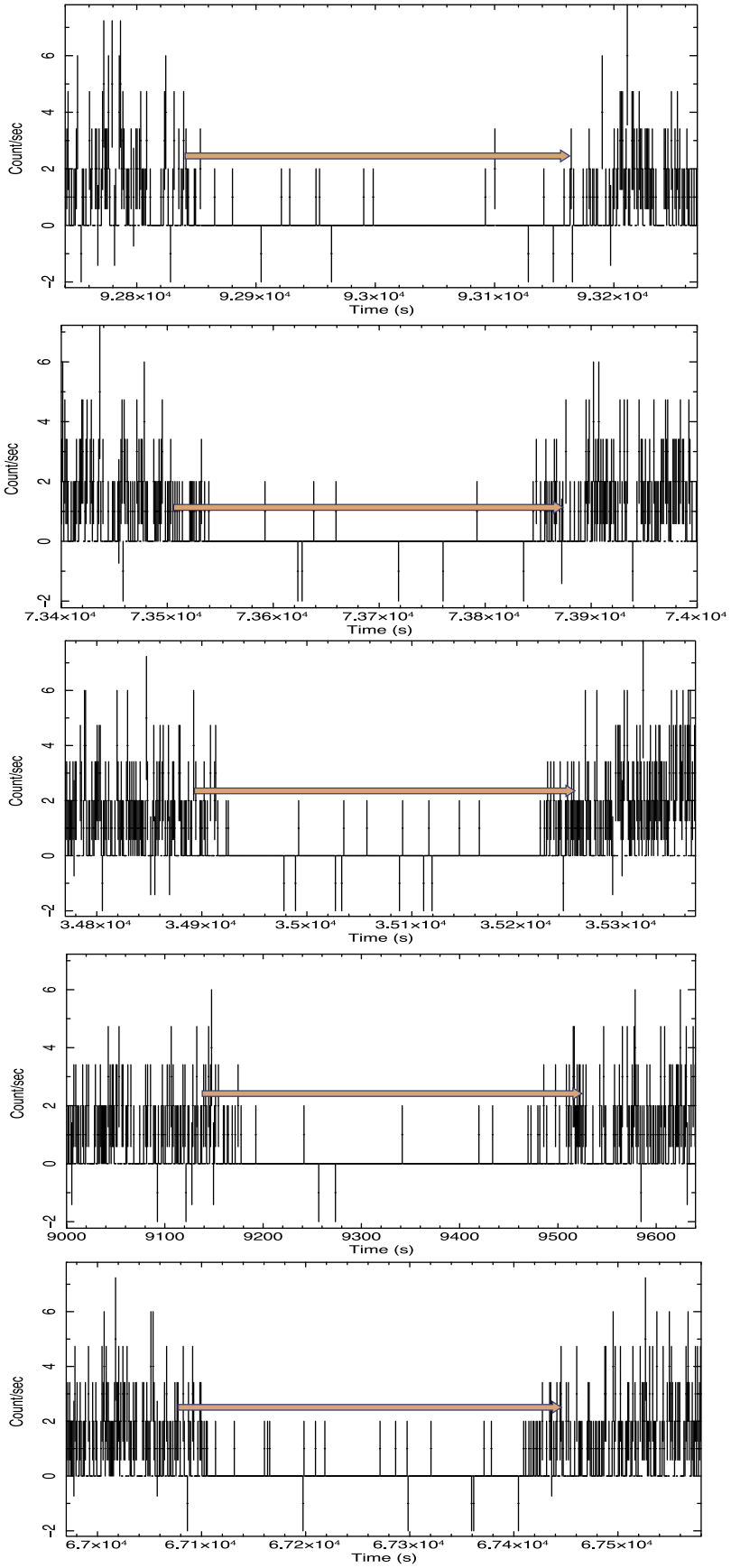

Figure 1. The quiescent X-ray light curve of Z Cha obtained using the XMM-Newton EPIC pn data. The figure shows the locations of the X-ray/optical eclipses in the X-ray light curve. A bin size of 1 s is used in accordance with the source count rate of 1.1 c s^{-1}, which yields approximately one photon per bin in the figure. A light orange color bar, indicating the X-ray eclipse duration of 324 s (from mid-ingress to mid-egress), calculated by A. A. Nucita et al. (2011), is approximately overlaid on the plots.

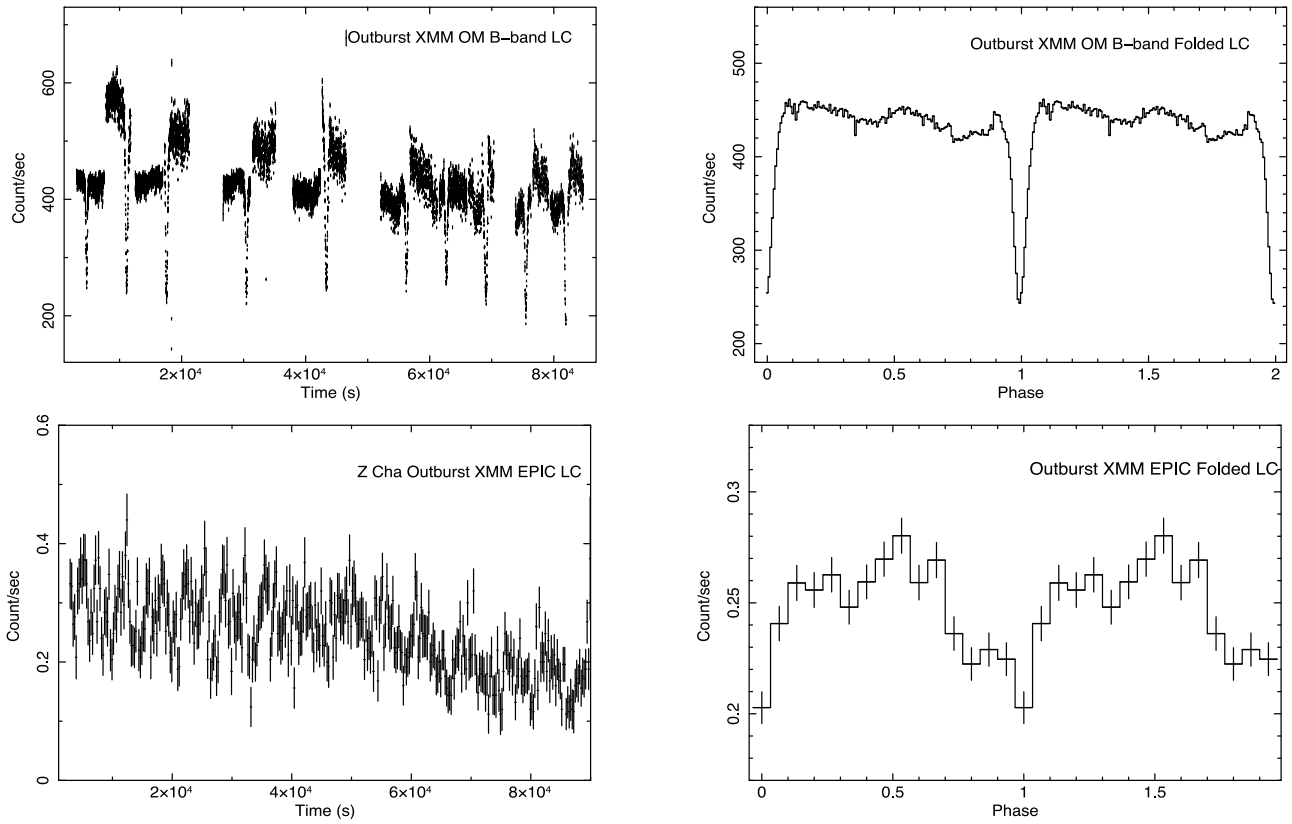

Figure 2. Optical OM *B* band (upper left) and X-ray light curve (LC; lower left), as observed by EPIC using XMM-Newton (both LCs are of the outburst). 10 s time binning is used for the *B*-band LC, while 250 s binning is used for the X-ray LC. The right panels show the LC in the outburst folded at the orbital period of Z Cha (see the text for Ephemerides). 150 and 15 phase bins are used for the *B*-band and X-ray EPIC mean LCs, respectively.

calculate the neutral hydrogen column in the line of sight: (1) COLDEN[13] (using J. M. Dickey & F. J Lockman 1990); and (2) *nhtot*[14](using R. Willingale et al. 2013). R. Willingale et al. (2013) calculate the molecular hydrogen column density, N(H2), in the Milky Way using a function that depends on the product of the atomic hydrogen column density, N(H I), and dust extinction, $E(B-V)$, with the aid of 21 cm radio emission maps and Swift gamma-ray burst data. Using these softwares, we found $N_{\rm H}$ in a range 1.08–1.36 $\times$ 10^{21} cm^{-2}. Our $N_{\rm H}$ value measured with QFit-1 in Table 1 is consistent with interstellar $N_{\rm H}$.

Next, we used a different absorption model and additional components to improve QFit-1, since it had relatively high χ^2_ν. QFit-2 was constructed with a partially covering absorber model that could reveal the existence of intrinsic absorption in the system, since Z Cha is a high-inclination eclipsing system. The *pcfabs* measured a partial covering of $77.0^{+5.0}_{-2.0}$% with about twice the interstellar value of cold absorption in the line of sight. We calculated that QFit-2 improved over QFit-1 using an F-TEST[15] within XSPEC that compares the χ^2 values and degrees of freedom (dof) of the two different fits. The F-TEST probability (1−confidence level) was 2.8×10^{-24}, which yields an improvement over 10σ.

In addition, we tested the possibility of existence of a power-law component, which may be due to scattering in the system, as was found for some NLs and DNe in outburst (Ş. Balman 2014, 2015; Ş. Balman et al. 2022; A. Dobrotka et al. 2023). We used the model (*pcfabs* $\times$ (*powerlaw* + CEVMKL)) for QFit-3, which yielded a better χ^2_ν that strongly suggested the existence of a power-law component in quiescence. The improvement of QFit-3 over QFit-2 was around the 10σ significance level, as well (the F-TEST probability was 2.4×10^{-14}). The spectrum fit with this model is displayed in the middle panel of Figure 3. QFit-1 to QFit-3 indicate a collisionally ionized cooling flow type of plasma (that has a temperature distribution), with $kT_{\rm max}$ in a range 9.8–13.0 keV. The α parameter (power-law index) of the temperature distribution is found to be different than 1.0, between 1.7 and 2.5, which indicates a hard-X-ray excess.

Furthermore, we tested the consistency of the EPIC spectra with nonequilibrium ionization plasma emission using the VNEI model in XSPEC. QFit-4 is similar to QFit-3 with only a replacement of the CEVMKL model with the VNEI model. The fit result does not improve upon QFit-3. However, we note here that the dof used in the fits are generally high, as a result of the simultaneous fitting of the three EPIC spectra. This yields significant differences in the fits even for a small variation in χ^2, which may not reflect physical differences, so that QFit-3 and QFit-4 are equivalent given the moderate spectral resolution. QFit-5 and QFit-6 are constructed to test the validity of a power-law component of emission and the existence of complex absorption, as in cold partially covering absorbers or warm photoionized absorbers. The fits are performed with a composite model of (*pcfabs* $\times$ *zxipcf* $\times$ VNEI), QFit-5, and

[13] http://cxc.harvard.edu/toolkit/colden.jsp
[14] http://www.swift.ac.uk/analysis/nhtot/index.php
[15] https://heasarc.gsfc.nasa.gov/xanadu/xspec/manual/node82.html

Table 1
Spectral Parameters of the Fits to the Quiescent EPIC Spectra of Z Cha

Model	Parameter	QFit-1	QFit-2	QFit-3	QFit-4	QFit-5	QFit-6
tbabs	$N_{\rm H}$ (10^{22}) (ato. cm^{-2})	$0.11^{+0.01}_{-0.01}$	N/A	N/A	N/A	N/A	N/A
pcfabs	$N_{\rm H}$ (10^{22}) (ato. cm^{-2})	N/A	$0.23^{+0.07}_{-0.06}$	$0.22^{+0.30}_{-0.20}$	$0.13^{+0.05}_{-0.06}$	$0.12^{+0.02}_{-0.01}$	$0.18^{+0.01}_{-0.02}$
	Cov. Frac.	N/A	$0.77^{+0.02}_{-0.02}$	$0.77^{+0.05}_{-0.02}$	$0.88^{+0.03}_{-0.03}$	$0.89^{+0.05}_{-0.03}$	$0.88^{+0.01}_{-0.02}$
zxipcf	$N_{\rm H}$ (10^{22}) (ato. cm^{-2})	N/A	N/A	N/A	N/A	$4.8^{+1.1}_{-1.4}$	$10.3^{+0.7}_{-0.7}$
	Log(ξ)	N/A	N/A	N/A	N/A	$3.56^{+0.10}_{-0.06}$	$1.91^{+0.04}_{-0.10}$
	Cov. Frac.	N/A	N/A	N/A	N/A	$0.54^{+0.03}_{-0.08}$	$0.36^{+0.01}_{-0.01}$
CEVMKL	α	$2.5^{+0.3}_{-0.4}$	$1.7^{+0.1}_{-0.3}$	$1.95^{+0.13}_{-0.12}$	N/A	N/A	$1.83^{+0.04}_{-0.05}$
	$kT_{\rm max}$ (keV)	$10.4^{+0.6}_{-0.6}$	$11.6^{+1.4}_{-0.3}$	$7.9^{+0.5}_{-0.5}$	N/A	N/A	$7.30^{+0.13}_{-0.11}$
	$K_{\rm cevmkl}$ ($\times10^{-3}$)	$9.7^{+2.0}_{-0.1}$	$7.8^{+0.8}_{-0.9}$	$6.5^{+0.7}_{-1.5}$	N/A	N/A	$12.4^{+0.1}_{-0.1}$
VNEI	τ (10^{11} s cm^{-3})	N/A	N/A	N/A	$5.4^{+0.6}_{-0.3}$	$2.9^{+0.1}_{-0.1}$	N/A
	kT (keV)	N/A	N/A	N/A	$5.5^{+0.1}_{-0.1}$	$8.4^{+0.2}_{-0.2}$	N/A
	$K_{\rm vnei}$ ($\times10^{-3}$)	N/A	N/A	N/A	$1.70^{+0.02}_{-0.06}$	$2.08^{+0.02}_{-0.01}$	N/A
	O/O$_\odot$	1.0 (fixed)	$1.4^{+0.3}_{-0.2}$	$1.3^{+0.3}_{-0.2}$	$0.6^{+0.4}_{-0.3}$	$1.9^{+0.5}_{-0.6}$	$0.40^{+0.20}_{-0.15}$
	Ne/Ne$_\odot$	$2.6^{+0.5}_{-0.5}$	$1.3^{+0.4}_{-0.4}$	$1.1^{+0.3}_{-0.5}$	$3.9^{+0.6}_{-0.6}$	$7.4^{+1.0}_{-1.0}$	$0.6^{+0.2}_{-0.3}$
	Si/Si$_\odot$	$1.9^{+0.3}_{-0.3}$	$1.3^{+0.2}_{-0.2}$	$1.6^{+0.2}_{-0.3}$	$1.4^{+0.2}_{-0.2}$	$0.7^{+0.2}_{-0.1}$	$1.13^{+0.14}_{-0.15}$
	S/S$_\odot$	$2.7^{+0.5}_{-0.4}$	$2.04^{+0.30}_{-0.30}$	$2.3^{+0.4}_{-0.3}$	$1.2^{+0.2}_{-0.2}$	$0.8^{+0.1}_{-0.2}$	$1.15^{+0.20}_{-0.19}$
	Fe/Fe$_\odot$	$0.80^{+0.05}_{-0.04}$	$0.80^{+0.04}_{-0.04}$	$0.90^{+0.02}_{-0.07}$	$0.70^{+0.05}_{-0.02}$	$0.70^{+0.02}_{-0.05}$	$0.52^{+0.03}_{-0.02}$
Power law	Phot. Ind.	N/A	N/A	$1.30^{+0.15}_{-0.10}$	$1.26^{+0.03}_{-0.02}$	N/A	N/A
	$K_{\rm power}$ ($\times10^{-4}$)	N/A	N/A	$1.3^{+1.0}_{-0.2}$	$1.35^{+0.09}_{-0.08}$	N/A	N/A
	$\chi^2_\nu(\nu)$	1.23 (1403)	1.14 (1401)	1.09 (1399)	1.13 (1399)	1.12 (1398)	1.00 (1398)
Flux	(10^{-12}) (erg cm^{-2} s^{-1})	$5.2^{+0.2}_{-0.5}$	$5.0^{+1.0}_{-0.2}$	$5.1^{+1.4}_{-0.8}$	$5.1^{+0.3}_{-0.3}$	$5.1^{+0.1}_{-0.1}$	$6.6^{+0.6}_{-0.3}$
Luminosity	(10^{30} erg s^{-1})	$5.5^{+0.3}_{-0.5}$	$5.3^{+1.1}_{-0.2}$	$5.4^{+1.5}_{-0.8}$	$5.8^{+0.3}_{-0.3}$	$5.8^{+0.1}_{-0.1}$	$7.5^{+0.6}_{-0.3}$
Flux$_{\rm thermal}$	(10^{-12}) (erg cm^{-2} s^{-1})	$5.2^{+0.2}_{-0.5}$	$5.0^{+1.0}_{-0.2}$	$3.2^{+0.8}_{-0.5}$	$3.6^{+0.2}_{-0.1}$	$5.1^{+0.1}_{-0.1}$	$6.6^{+0.6}_{-0.3}$
$L_{\rm thermal}$	(10^{30} erg s^{-1})	$5.5^{+0.3}_{-0.5}$	$5.3^{+1.1}_{-0.2}$	$3.4^{+0.9}_{-0.6}$	$4.1^{+0.2}_{-0.1}$	$5.8^{+0.1}_{-0.1}$	$7.5^{+0.6}_{-0.3}$
Flux$_{\rm power}$	(10^{-12}) (erg cm^{-2} s^{-1})	N/A	N/A	$2.0^{+0.8}_{-0.7}$	$1.5^{+0.2}_{-0.2}$	N/A	N/A
$L_{\rm power}$	(10^{30} erg s^{-1})	N/A	N/A	$2.1^{+0.9}_{-0.7}$	$1.7^{+0.2}_{-0.2}$	N/A	N/A

Note. Fits are performed using EPIC pn and MOS data in the 0.3–10.0 keV range. A constant-value model is fitted as a free parameter to account for the normalization between different detectors. $N_{\rm H}$ is the absorbing column. α is the index of the power-law emissivity function ($d{\rm EM} = (T/T_{\rm max})^{\alpha-1}\,dT/T_{\rm max}$). $T_{\rm max}$ is the maximum temperature for the CEVMKL model. $K_{\rm CEVMKL}$ is the normalization for the CEVMKL model; $K = (10^{-14}/4\pi D^2) \times {\rm EM}$, where EM (emission measure) $= \int n_e\, n_{\rm H}\, dV$ (the integration is over the emitting volume V). $K_{\rm powerlaw}$ is the normalization (i.e., the photon flux in phot. cm^{-2} s^{-1}) for the power-law model. The NEIvers.3.0.9 plasma code with the ATOMDB database was assumed for the VNEI fits. All errors are calculated at the 90% confidence limit for a single parameter. The unabsorbed X-ray flux and the luminosities are given in the range 0.2–10.0 keV. The distance of 97 pc is used for luminosity calculations.

(*pcfabs* × *zxipcf* × CEVMKL), QFit-6. The spectrum fit with QFit-5 is shown in the right panel of Figure 3. The χ^2_ν values improve upon the fits with the power laws (when tested with the F-TEST), suggesting that there are complex absorption components on the existing plasma emission of collisional equilibrium (CIE) or nonequilibrium origin. The power-law model may not be physical and may only be providing a modification of the continuum, reducing χ^2. We note here that, as mentioned before, the power-law components are detected in the high states. We find that the $N_{\rm H}$ values of the partial covering of the cold absorber are consistent with interstellar absorption in these fits, whereas the ionized warm absorber shows a lower covering fraction ($54.0^{+3.0}_{-8.0}$% for VNEI and $36.0^{+1.0}_{-1.0}$% for CEVMKL), with equivalent hydrogen column density of $4.80^{+1.10}_{-0.06} \times 10^{22}$ cm^{-2} for VNEI and larger for the fit with the CEVMKL model, $10.3^{+0.7}_{-0.7} \times 10^{22}$ cm^{-2}. These values are a factor of 40–80 times more than the intrinsic and/or line-of-sight cold absorption. QFit-5 and QFit-6 indicate a plasma temperature of $8.4^{+0.2}_{-0.2}$ keV for the VNEI model and $kT_{\rm max} = 7.30^{+0.13}_{-0.11}$ keV for the CEVMKL model fits.

All unabsorbed fluxes for the fits between 0.2 and 10.0 keV are given in Table 1 with the calculated X-ray luminosities, using the 97 pc source distance (J. Wood et al. 1986). We find most elemental abundances to be consistent with solar, except for some possible overabundance of Ne/Ne$_\odot$ = (1.1–7.4) and S/S$_\odot$ = (1.2–2.7) and underabundance of Fe/Fe$_\odot$ = (0.5–1.0) and perhaps O/O$_\odot$ = (0.3–1.9). We have checked if the underabundance of iron has to do with iron absorption lines

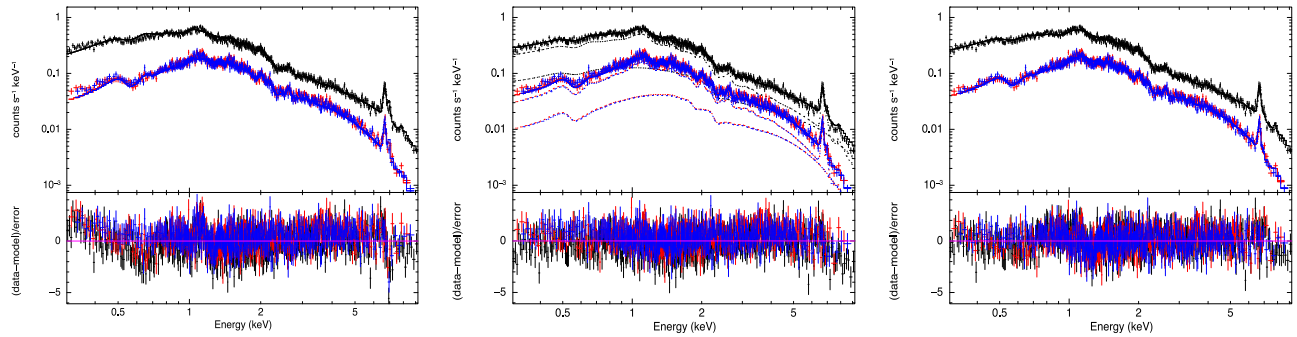

Figure 3. Left: the quiescent EPIC pn and MOS1 and MOS2 spectra of Z Cha simultaneously fit with the (*tbabs* × CEVMKL) model. Middle: the EPIC spectra simultaneously fit with the composite model of (*pcfabs* × (CEVMKL + *power*)). Right: the spectra fit using the composite model (*pcfabs* × *zxipcf* × VNEI). In the panels, the dotted lines show the contribution of the different model components. The lower panels show the residuals in standard deviations (in σ).

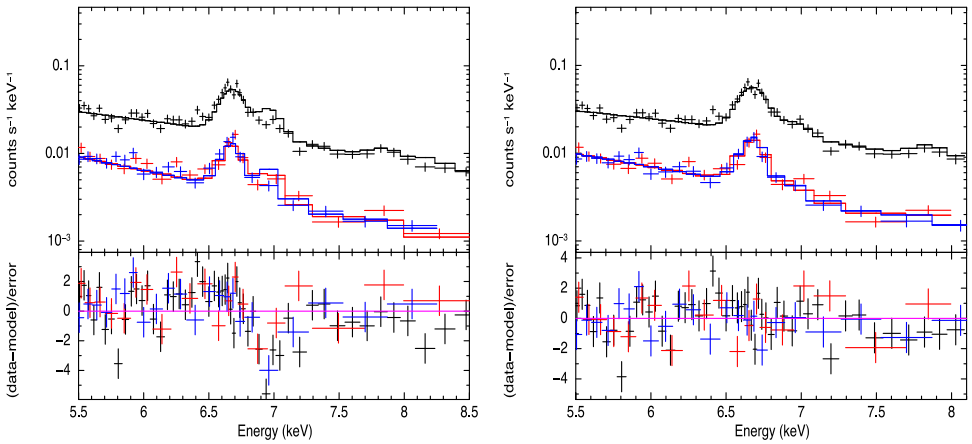

Figure 4. Simultaneously fitted EPIC spectra with the model (*tbabs* × CEVMKL). The plots show the fit quality and residuals around the iron complex at 6–7 keV. The residuals on the left reveal an apparent H-like iron absorption line. The iron abundance is thawed in the fitting process. The right panel is a fit using the *warmabs* model—partially ionized (photoionized) absorber—where the absorption line is well accommodated by the absorber model (see Section 5.2).

within the 6–7 keV band. The left panel of Figure 3 indicates significant departures in the residuals around the Fe XXV and Fe XXVI complex, where the (*tbabs* × CEVMKL) model was used. The inclusion of a power law or a partially ionized absorber (*zxipcf*) model alleviates this problem, but the Fe abundance seems to be problematic. To test the existence of an iron absorption line, we included a Gaussian absorption line in the fitting procedure in the 6.6–7.0 energy range along the (*tbabs* × CEVMKL) model, which improved the residuals considerably in the 6.0–7.0 keV band (also the χ^2_ν). This line is found at $6.95^{+0.05}_{-0.05}$ keV, showing that this is an Fe XXVI absorption line (an H-like iron absorption line), with a line depth of $0.12^{+0.04}_{-0.06}$ (unitless) and a line width (σ) of $0.09^{+0.01}_{-0.04}$ keV. Figure 4 shows the region of the spectra where the Fe XXV and Fe XXVI emission lines are present and the H-like iron absorption line is detected using the CEVMKL model. The left panel shows the fit (*tbabs* × CEVMKL) in which iron abundance is thawed, yielding iron underabundance. An Fe XXVI absorption line is detected with residual deviations at about 4σ. This fit is irrespective of the plasma emission model used, such as MKCFLOW or APEC in XSPEC. The inclusion of a *power-law* model diminishes the temperatures and the fitted continuum is modified, reducing the residual variations at the line energy and improving the fits, while the *zxipcf* model alleviates the absorption feature to a good extent, diminishing the residual effects. Thus, the iron absorption line is not as apparent in the middle and right panels of Figure 3. The right panel of Figure 4 shows the vicinity of the iron lines when the *warmabs* model is used as a multiplicative partially ionized (photoionized) absorption model (see Section 5.2). On the other hand, the VNEI model, which is a nonequilibrium ionization plasma model, has a weak Fe XXVI emission line and a fit with VNEI yields only a (1.5–2) σ dip at the absorption-line energy and the detection is then not very significant.

Utilizing the same quiescent XMM-Newton EPIC data set, A. A. Nucita et al. (2011) found a best fit with $\chi^2_\nu = 1.8$ (for 628 dof), using a composite model of cold absorption and *absori*, an old version of a photoionized absorber model, and CEMEKL (a multitemperature plasma emission model similar to CEVMKL, with only the metal abundances Z to vary). These fits revealed $N_{\rm H} = (5.8 \pm 0.4) \times 10^{20}\,{\rm cm}^{-2}$ for the neutral hydrogen column density and $N_{\rm H} = 1.7 \pm 0.1 \times 10^{21}\,{\rm cm}^{-2}$ for the equivalent ionized hydrogen column density, for an ionized absorber with $\xi = 0.3 \pm 0.1$. We find considerably different values for these parameters. A. A. Nucita et al. (2011) find a multitemperature plasma with $\alpha = 1.6 \pm 0.1$ for the power-law index of the temperature distribution with $kT_{\rm max} = 11.4 \pm 0.2$ keV. We note that the maximum temperature and the α parameter are similar to some of our fits (i.e., QFit-2) with the partially covering absorber model. However, the partially covering cold and warm absorbers we find are very different. The χ^2_ν values we obtain from any of the fits in Table 1 are significantly better than the fit in A. A. Nucita et al. (2011), thus we have improved it.

In addition, we have investigated the data for the two orbital phases, 0.30 ± 0.02 and 0.73 ± 0.02, noted by A. A. Nucita et al. (2011) as showing dipping behavior in the mean X-ray light curve. Using the SAS task *phasecalc*, we calculated the phases of the photon arrival times utilizing the ephemerides of R. Baptista et al. (2002). Then, we extracted spectral filtering on these calculated phases and conducted spectral analysis using QFit-5 in Table 1, with the VNEI plasma model. The spectral fit between phases 0.35 and 0.25 indicates similar parameters as the phase-average fit of the plasma model and the partially covering cold/neutral absorber. The partially ionized absorber has a similar ionization parameter of $\log(\xi) = 3.5$–3.7 but yields an equivalent $N_{\rm H} = (8.2$–$21.0) \times 10^{22}\,{\rm cm}^{-2}$ that is two to four times larger than the phase-average result with a partial covering of >87%. The spectral fit of the spectrum for phases 0.7–0.8 gives similar plasma model parameters, but with different absorption characteristics. The cold partially covering absorber is two times larger and the partially ionized absorber is colder (less ionized), with $\log(\xi) = 0.1$–0.3 and equivalent $N_{\rm H} = (1.0$–$1.4) \times 10^{22}\,{\rm cm}^{-2}$ (the partial covering is (70–80)%). The error ranges are at the 90% confidence level and the χ^2_ν of the two fits are 1.2 (dof 159) and 1.0 (dof 97), respectively. The iron abundance in these two fits is found to be between 1.5 and 2.5 times the solar value, which is larger than any fit result attained in our analysis.

4.2. Analysis of EPIC Data in Outburst

The background and source spectra along with the response and ancillary files for the outburst data of Z Cha were generated as described in Section 2. The EPIC spectra were grouped with a minimum of 70, 45, and 45 counts in each spectral bin for pn, MOS1, and MOS2, respectively, to achieve good χ^2 statistics in the fitting procedure. The spectra are analyzed using the HEASoft and XSPEC softwares, as described in Section 4.1, for the analysis of data obtained in quiescence.

For the spectral analysis of the EPIC data obtained in outburst, the same absorption models and plasma emission model components are utilized, except for an additional blackbody model BBODY in XSPEC. As in the analysis of data obtained in quiescence, we have used the multi-temperature isobaric cooling flow type of plasma emission model CEVMKL in XSPEC, with switch = 2, and the model VNEI, the nonequilibrium ionization plasma model in XSPEC, when performing simultaneous fits to the EPIC spectra (pn, MOS1, and MOS2). A constant-value model is also fit along with the composite models to account for cross-normalization calibration between the different detectors. Four composite models are constructed as OFit-1 to OFit-4 (see Table 2). The resulting parameters of the spectral fits are given in Table 2 for these four models. These composite models do not include the plasma model VNEI (the nonequilibrium ionization plasma model), because the fits can never reproduce the 6–7 keV single iron line correctly in the fitting process with χ^2_ν larger than 2.0. This may mean that this iron line is produced in a plasma in CIE or the iron line is not at its rest/expected wavelength for the VNEI model; this will be elaborated in the discussion section. Thus, all fits involve the CEVMKL model plasma emission for simplicity. However, the α parameter of the temperature distribution is ~0.01, similar to the case of NL systems (high-state CVs) that bear nonstandard advective hot flows. This will be elaborated in the discussion section as well. Example spectral fits with the CEVMKL plasma model are displayed in Figure 5 for OFit-1, OFit-3, and OFit-4.

The general theoretical expectation of a DN outburst is the existence of a blackbody emission component in the X-ray regime from an optically thick standard BL as the accretion rate increases toward the WD in the disk. Thus, we have constructed a composite model fit OFit-1 with a model of BBODY (in XSPEC); (*tbabs* × (BBODY + GAUSS + CEVMKL + *power*)). This yields an acceptable χ^2_ν, where the addition of the BBODY model improves the fit at only at 93% confidence level when an F-TEST is used. A *power-law* emission component is also necessary to reduce the χ^2_ν level of the fit, OFit-1. However, the CEVMKL plasma emission model does not reproduce the iron emission line (in the 6–7 keV band) properly and an additional GAUSS emission-line model is added to account for this inadequacy at $6.64^{+0.06}_{-0.07}$ keV. This line is a narrow line constrained with the spectral resolution of EPIC, which indicates an He-like iron line with a flux of $1.0^{+0.4}_{-0.3} \times 10^{-14}\,{\rm erg\,cm^{-2}\,s^{-1}}$, which is consistent with the low X-ray temperature. The plasma temperatures derived from the CEVMKL models are $kT_{\rm max} = 0.97$–3.20 keV, given $\chi^2_\nu < 1.3$ (from all fits). The composite model OFit-4 is constructed (*pcfabs* × *pcfabs* × (*GAUSS* + *CEVMKL* + *power*)) to test if the plausible soft-X-ray component (BBODY—blackbody emission component) is a manifestation of the absorption components in the system. This model lacks the BBODY component, but has two partially covering cold absorber components. The χ^2_ν level of this fit is as good as the model with the BBODY component, suggesting that the BBODY model may be accounting for incorrect absorption modeling. We note that both of the detected cold absorbers are not high enough to completely disguise/absorb the blackbody emission component in OFit-1. Thus, the existence of a blackbody-emitting BL cannot be asserted based on the EPIC data in outburst.

OFit-3 (*pcfabs* × *pcfabs* × *zxipcf* × (*CEVMKL*)) is constructed to reveal the existence of cold and photoionized warm absorption in the system along with the CEVMKL plasma model. The fit yields the best-fitting model (see Table 2). Therefore, there is complex absorption in the system, where one of the cold partially covering absorber components is similar to the one in quiescence, while the second one is larger by a factor of 15, $(8.7$–$10.7) \times 10^{22}\,{\rm cm}^{-2}$. The warm absorption modeled by the *zxipcf* component shows a very large equivalent $N_{\rm H} = (2.30$–$2.95) \times 10^{24}\,{\rm cm}^{-2}$ with an ionization parameter $\log(\xi)$ in a range 2.79–2.83 (the covering fraction is 90%). This partially covering warm absorption is about a factor of 25–50 times more than in quiescence. This is the only fit with the CEVMKL model where the He-like weak iron line is adequately fit by the plasma emission model (no need for an additional GAUSS model).

4.3. High-resolution X-Ray Spectroscopy with RGS

The basic analysis steps of the XMM-Newton RGS data of Z Cha have been outlined in Section 2. The SAS tasks *rgsproc* and *rgscombine* are used to derive spectra of different orders (1, 2) using default extraction regions and to coadd RGS1 and RGS2 spectra (order 1) to make a total average spectrum with good statistics and high energy resolution ($\lambda/\Delta\lambda \sim 200$–$800$).[16] The inferred tasks also create the necessary background spectra and

[16] https://xmm-tools.cosmos.esa.int/external/xmm_user_support/documentation/uhb/rgs.html

Table 2
Spectral Parameters of the Fit to the Outburst EPIC Spectra of Z Cha

Model	Parameter	OFit-1	OFit-2	OFit-3	OFit-4
tbabs	$N_{\rm H}$ (10^{22} ato. cm^{-2})	$0.08^{+0.01}_{-0.01}$	N/A	N/A	N/A
pcfabs	$N_{\rm H}$ (10^{22} ato. cm^{-2})	N/A	$4.1^{+0.7}_{-0.6}$	$9.6^{+1.1}_{-0.9}$	$0.56^{+0.09}_{-0.10}$
	Cov. Frac.	N/A	$0.47^{+0.05}_{-0.03}$	$0.78^{+0.02}_{-0.02}$	$0.63^{+0.08}_{-0.06}$
pcfabs	$N_{\rm H}$ (10^{22} ato. cm^{-2})	N/A	N/A	$0.19^{+0.01}_{-0.02}$	$0.12^{+0.3}_{-0.3}$
	Cov. Frac.	N/A	N/A	$0.70^{+0.03}_{-0.03}$	$0.4^{+0.3}_{-0.1}$
zxipcf	$N_{\rm H}$ (10^{22} ato. cm^{-2})	N/A	N/A	$261.1^{+34.0}_{-31.0}$	N/A
	Log(ξ)	N/A	N/A	$2.81^{+0.02}_{-0.02}$	N/A
	Cov. Frac.	N/A	N/A	$0.90^{+0.02}_{-0.01}$	N/A
CEVMKL	α	<0.1	<0.02	<0.07	<0.09
	$kT_{\rm max}$ (keV)	$1.12^{+0.08}_{-0.06}$	$8.9^{+0.2}_{-0.9}$	$3.0^{+0.2}_{-0.2}$	$1.01^{+0.05}_{-0.04}$
	$K_{\rm cevmkl}$ ($\times10^{-4}$)	$2.7^{+0.1}_{-0.1}$	$2.5^{+0.1}_{-0.1}$	$77.0^{+2.0}_{-2.0}$	$5.6^{+0.3}_{-0.1}$
BBODY	$kT_{\rm BB}$ (keV)	$0.027^{+0.008}_{-0.006}$	N/A	N/A	N/A
	$K_{\rm BB}$ ($\times10^{-4}$)	$3.0^{+2.5}_{-0.7}$	N/A	N/A	N/A
	O/O$_\odot$	$0.8^{+0.1}_{-0.1}$	$0.90^{+0.05}_{-0.04}$	$0.95^{+0.06}_{-0.05}$	$0.8^{+0.1}_{-0.1}$
	Ne/Ne$_\odot$	$1.3^{+0.2}_{-0.2}$	$0.7^{+0.2}_{-0.2}$	$2.0^{+0.2}_{-0.2}$	$1.1^{+0.2}_{-0.2}$
	Mg/Mg$_\odot$	$1.2^{+0.2}_{-0.1}$	$2.3^{+0.3}_{-0.3}$	$1.3^{+0.2}_{-0.2}$	$0.8^{+0.1}_{-0.1}$
	Si/Si$_\odot$	$1.3^{+0.2}_{-0.2}$	$1.8^{+0.3}_{-0.3}$	$1.50^{+0.02}_{-0.02}$	$0.8^{+0.1}_{-0.1}$
	S/S$_\odot$	$2.4^{+0.7}_{-0.7}$	$0.9^{+0.3}_{-0.3}$	$1.3^{+0.3}_{-0.3}$	$1.4^{+0.3}_{-0.4}$
	Fe/Fe$_\odot$	$0.6^{+0.1}_{-0.1}$	$1.14^{+0.04}_{-0.04}$	$0.60^{+0.02}_{-0.07}$	$0.6^{+0.1}_{-0.1}$
Power law	Phot. Ind.	$1.6^{+0.1}_{-0.1}$	N/A	N/A	$1.56^{+0.08}_{-0.12}$
	$K_{\rm power}$ ($\times10^{-5}$)	$3.7^{+0.2}_{-0.2}$	N/A	N/A	$3.4^{+0.1}_{-0.2}$
GAUSS	Line Energy (keV)	$6.64^{+0.06}_{-0.05}$	N/A	N/A	$6.64^{+0.06}_{-0.07}$
	Sigma (keV) ($\times10^{-3}$)	$6.1^{+94.0}_{-\infty}$	N/A	N/A	$6.7^{+90.0}_{-\infty}$
	$K_{\rm Gauss}$ ($\times10^{-7}$)	$9.6^{+3.7}_{-3.3}$	N/A	N/A	$9.6^{+3.6}_{-3.4}$
	$\chi^2_\nu(\nu)$	1.31 (449)	1.46 (454)	1.24 (450)	1.29 (448)
Flux	(10^{-12}) (erg cm^{-2} s^{-1})	$2.5^{+6.2}_{-1.2}$	$1.3^{+0.1}_{-0.1}$	$28.0^{+1.0}_{-8.0}$	$1.7^{+0.1}_{-0.1}$
Luminosity	(10^{30} erg s^{-1})	$2.9^{+7.0}_{-1.4}$	$1.50^{+0.03}_{-0.13}$	$32.0^{+1.0}_{-0.9}$	$1.9^{+0.2}_{-0.1}$
Flux$_{\rm thermal}$	(10^{-13}) (erg cm^{-2}s^{-1})	$7.7^{+0.5}_{-0.6}$	$13.0^{+1.0}_{-1.0}$	$280.0^{+10.0}_{-80.0}$	$13.8^{+1.2}_{-0.8}$
$L_{\rm thermal}$	(10^{29} erg s^{-1})	$8.8^{+0.6}_{-0.7}$	$15.0^{+0.3}_{-1.3}$	$320.0^{+10.0}_{-9.0}$	$15.7^{+1.4}_{-1.0}$
Flux$_{\rm power}$	(10^{-13}) (erg cm^{-2} s^{-1})	$2.9^{+0.5}_{-0.3}$	N/A	N/A	$2.8^{+0.2}_{-0.1}$
$L_{\rm power}$	(10^{29} erg s^{-1})	$3.3^{+0.6}_{-0.3}$	N/A	N/A	$3.2^{+0.2}_{-0.1}$
Flux$_{\rm BB}$	(10^{-11}) (erg cm^{-2} s^{-1})	$1.2^{+1.7}_{-0.7}$	N/A	N/A	N/A
$L_{\rm BB}$	(10^{31} erg s^{-1})	$1.3^{+2.1}_{-0.7}$	N/A	N/A	N/A

Note. Fits are performed using EPIC pn and MOS data in the 0.3–10.0 keV range. A constant value is fitted as a free parameter to account for the normalization between different detectors. For descriptions of the models, parameters, and normalizations, please refer to Table 1. $K_{\rm BB}$ is the normalization of the blackbody model in units of L_{39}/D_{10}, where L_{39} is the source luminosity in units of 10^{39} erg s^{-1} and D_{10} is the distance to the source in units of 10 kpc. $K_{\rm Gauss}$ is the normalization for the Gaussian emission-line model (it is the flux of the line in phot. cm^{-2} s^{-1}). All errors are given at the 90% confidence limit for a single parameter. The unabsorbed X-ray flux and the luminosities are given in the range 0.2–10.0 keV, except for the blackbody model, where the ranges are for 0.1–10.0 keV. For luminosities, a distance of 97 pc is assumed.

response files (for individual or combined spectra). The spectral analysis is performed within the XSPEC software (for references and model descriptions, see K. A. Arnaud 1996). The RGS spectra are marginally grouped by three to six channels in the range 1–4000 to improve the χ^2 statistics for the fits, mitigating for the best energy resolution. In addition, for the individual line fits using a Gaussian model, the binning has been changed to minimum counts of 10–15 in each spectral bin, when necessary.

The RGS data analysis is utilized mainly for line diagnostics and to confirm the spectral results of the EPIC analysis. We note that the count rates are lower and the statistical quality of the spectra is adequate, but the continuum is detected at a lower level, while the line emissions are of high significance compared to the EPIC data. We have fitted the quiescent and outburst RGS spectra with several composite models as in Sections 4.1 and 4.2. Table 3 displays the spectral parameters describing the quiescence and outburst RGS spectra of Z Cha, and Figure 6 shows examples of fitted spectra. For quiescence, we present two composite models: *pcfabs* × CEVMKL and *pcfabs* × *zxipcf* × VNEI. We used similar models for the outburst: *pcfabs* × *pcfabs* × CEVMKL and *pcfabs* × *zxipcf* ×

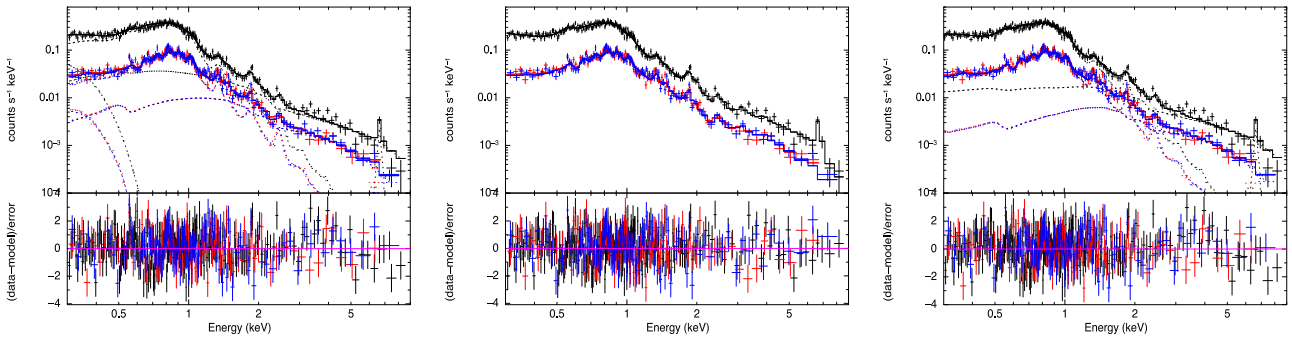

Figure 5. Fits to the outburst EPIC pn and MOS1 and MOS2 spectra of Z Cha. All three EPIC spectra are fit simultaneously with the (*tbabs* × (BBODY + GAUSS + CEVMKL + *power*)) model on the left. The middle panel shows the EPIC spectra simultaneously fit with the composite model of (*pcfabs* × *pcfabs* × *zxipcf* × CEVMKL). The right panel shows the same fit spectra using the composite model (*pcfabs* × *pcfabs* × (CEVMKL + *power*)). In the panels, the dotted lines show the contributions of the different model components. The lower panels show the residuals in standard deviations (σ).

Table 3
Spectral Parameters of the Fits to the Quiescent and Outburst Phases of the RGS Spectra of Z Cha

Model	Parameter	Quiescence-1	Quiescence-2	Outburst-1	Outburst-2
pcfabs	$N_{\rm H}$ (10^{22} atoms cm^{-2})	$0.14^{+0.03}_{-0.02}$	$0.14^{+0.02}_{-0.02}$	$0.12^{+0.05}_{-0.05}$	$0.6^{+0.2}_{-0.3}$
	Cov. Frac.	0.8<	0.85<	0.7<	$0.87^{+0.03}_{-0.10}$
pcfabs	$N_{\rm H}$ (10^{22} atoms cm^{-2})	N/A	N/A	$1.7^{+\infty}_{-0.6}$	N/A
	Cov. Frac	N/A	N/A	$0.78^{+0.10}_{-0.02}$	NA
zxipcf	$N_{\rm H}$ (10^{22} atoms cm^{-2})	N/A	$1.1^{+1.3}_{-0.6}$	N/A	$2.9^{+5.6}_{-2.1}$
	Log(ξ)	N/A	$3.6^{+0.4}_{-0.3}$	N/A	$2.8^{+0.4}_{-0.5}$
	Cov. Frac.	N/A	0.7 <	N/A	$0.5^{+0.1}_{-0.2}$
VNEI	kT (keV)	N/A	$4.7^{+0.7}_{-0.6}$	N/A	$0.6^{+0.1}_{-0.1}$
	τ (scm^{-3})	N/A	$8.7^{+\infty}_{-4.0} \times 10^{11}$	N/A	$1.1^{+0.3}_{-0.4} \times 10^{11}$
	$K_{\rm vnei}$	N/A	$1.8^{+0.1}_{-0.1} \times 10^{-3}$	N/A	$2.6^{+1.0}_{-1.3} \times 10^{-4}$
CEVMKL	α	$1.9^{+0.2}_{-0.2}$	N/A	$0.5^{+0.3}_{-0.4}$	N/A
	$kT_{\rm max}$ (keV)	$9.1^{+1.7}_{-1.2}$	N/A	$0.9^{+0.3}_{-0.2}$	N/A
	$K_{\rm cevmkl}$	$6.5^{+0.3}_{-0.4} \times 10^{-3}$	N/A	$9.5^{+0.6}_{-1.2} \times 10^{-4}$	N/A
	N/N$_\odot$	1.0 (fixed)	1.0 (fixed)	$3.6^{+2.3}_{-2.3}$	$3.1^{+2.3}_{-2.1}$
	O/O$_\odot$	$1.3^{+0.5}_{-0.4}$	$2.1^{+0.8}_{-0.6}$	$1.6^{+0.4}_{-0.4}$	$0.7^{+0.2}_{-0.2}$
	Ne/Ne$_\odot$	$2.2^{+1.2}_{-1.1}$	$3.3^{+1.5}_{-1.5}$	$1.9^{+1.2}_{-1.1}$	$1.2^{+0.5}_{-0.5}$
	Mg/Mg$_\odot$	$2.4^{+1.4}_{-1.2}$	$2.3^{+1.5}_{-1.5}$	1.0 (fixed)	1.0 (fixed)
	Si/Si$_\odot$	$3.6^{+3.0}_{-2.5}$	$3.6^{+3.5}_{-3.2}$	1.0 (fixed)	1.0 (fixed)
	Fe/Fe$_\odot$	$1.0^{+0.3}_{-0.3}$	$0.8^{+0.2}_{-0.3}$	$1.1^{+0.3}_{-0.2}$	$0.9^{+0.3}_{-0.2}$
	$\chi^2_\nu(\nu)$	1.18 (372)	1.22 (369)	1.29 (366)	1.31 (365)
Flux	(10^{-12} erg cm^{-2}s^{-1})	$4.1^{+0.6}_{-0.6}$	$4.0^{+0.4}_{-0.3}$	$2.2^{+1.7}_{-0.7}$	$1.3^{+0.9}_{-0.7}$
Luminosity	(10^{30} erg s^{-1})	$4.7^{+0.6}_{-0.7}$	$4.5^{+0.5}_{-0.3}$	$2.5^{+1.9}_{-0.8}$	$1.5^{+1.0}_{-0.8}$

Note. Fits are performed using RGS1 + 2 data in the 0.4–2.0 keV range. $N_{\rm H}$ is the absorbing column, α is the index of the power-law emissivity function of the CEVMKL model (with $d{\rm EM} = (T/T_{\rm max})^{\alpha-1} dT/T_{\rm max}$), $T_{\rm max}$ is the maximum temperature for the CEVMKL model, and $K_{\rm CEVMKL}$ is the normalization for the CEVMKL model. The NEIvers.3.0.9 plasma code with the ATOMDB database was assumed for the VNEI fits, and $K_{\rm VNEI}$ is the normalization for the VNEI model. All errors are calculated at the 90% confidence limit for a single parameter. The unabsorbed X-ray flux and the luminosities are given in the range 0.2–10.0 keV. To calculate the luminosities, a distance of 97 pc is assumed.

VNEI. The two plasma models have already been described in Section 4.1. Table 3 yields a good comparison of both phases of Z Cha as the source makes a state transition. We note that the two archival data sets that we analyze in outburst and quiescence are not contiguous.

The neutral absorption toward the source is modeled via *pcfabs* (partially covering neutral/cold absorber), which yields a range of values $(0.11–0.17) \times 10^{22}$ cm^{-2} with ∼95% fractional coverage, which is similar to the value in Table 1 derived from the EPIC results in quiescence. Thus, this value is also detected for the outburst stage as an absorption component, but the outburst shows the presence of more absorption in the form of a cold partially covering absorber and/or a warm/ionized (photoionized) absorber. We fitted the CEVMKL CIE plasma model along with the cold/neutral partially covering absorber, and we fitted the VNEI

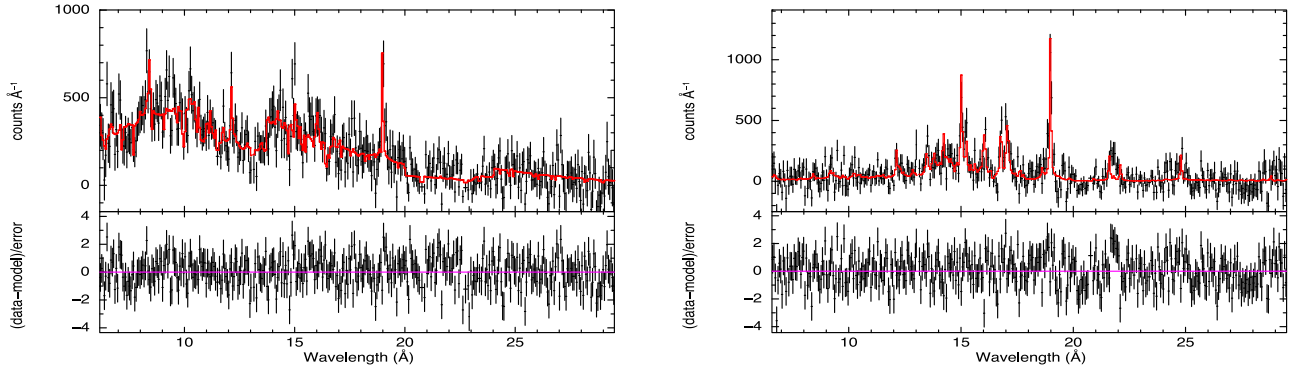

Figure 6. Averaged XMM-Newton RGS 1 and RGS 2 spectra of Z Cha. The left panel shows the high-resolution X-ray spectrum obtained in quiescence fitted with the (*pcfabs* × CEVMKL) model. The right panel shows the averaged RGS 1 and RGS 2 spectra of Z Cha in outburst fit with the (*pcfabs* × *pcfabs* × CEVMKL) composite model. In both panels, the solid lines (in red color) show the fitted model. The lower panels show the residuals in standard deviations (in σ).

nonequilibrium ionization plasma along with a partially ionized absorber model, *zxipcf*. The particular choices of absorption components and plasma models are made relying on the small χ^2_ν values, the goodness of the fits. For example, when a CEVMKL model is used in place of VNEI with the ionized absorber component, the resulting parameters of the ionized absorber are nonphysical for the outburst data. For quiescence, the χ^2_ν criterion is used to display the two best-fitting composite models. Other composite models do not provide any better fits to the quiescent RGS spectrum. The X-ray plasma temperatures found for the RGS spectra are in accordance with Table 1 (quiescence) and Table 2 (outburst). The X-ray plasma temperature in quiescence is 4.1–5.4 keV, using the VNEI model with the *zxipcf* absorber, and 7.9–10.8 keV, for the CEVMKL model using only a cold/neutral partially covering absorber. The X-ray plasma temperature in outburst is $kT_{\rm max} = 0.7$–1.2 keV (using the CEVMKL model with two partially covering cold absorbers) and 0.5–0.7 keV for the VNEI plasma model using two components of absorption (partially ionized and cold) with partial covering.

The outburst reveals a cold partially covering absorber with either $1.7^{+\infty}_{-0.6} \times 10^{22}\,{\rm cm}^{-2}$ (Outburst-1) or $(0.3$–$0.8) \times 10^{22}\,{\rm cm}^{-2}$ (Outburst-2). Moreover, a partially ionized absorber model with $2.9^{+5.6}_{-2.1} \times 10^{22}\,{\rm cm}^{-2}$ (Outburst-2) along with the VNEI plasma model is consistent with the coadded RGS spectrum. We note here that the EPIC spectral results in outburst yield considerably higher values for the partially ionized absorber in a range $(230.0$–$295.0) \times 10^{22}\,{\rm cm}^{-2}$ (see Table 2). The ionization parameters derived from the RGS spectra for the ionized absorption component are found to be $\log(\xi) = 3.6^{+0.4}_{-0.3}$ for quiescence and $\log(\xi) = 2.8^{+0.4}_{-0.5}$ for outburst. The α parameter (power-law index for the temperature distribution of the CEVMKL model) is found in accordance with the EPIC results; 1.7–2.1 for quiescence and 0.1–0.8 for outburst (similar to NLs). The ionization timescale for the VNEI plasma model yields values in a range of $8.7^{+\infty}_{-4.0} \times 10^{11}\,{\rm s\,cm}^{-3}$ for quiescence and $1.1^{+0.3}_{-0.4} \times 10^{11}\,{\rm s\,cm}^{-3}$ for outburst, revealing near-equilibrium plasma, but see also the next section on line detections. EPIC spectral analyses reveal ionization timescales that are different, with better statistical errors (better constrained) for the quiescence. The outburst will be elaborated in the discussion section. We have varied the abundances of N, O, Ne, Mg, Si, and Fe during the fits and found that they are close to solar values or slightly enhanced as a result of global fitting, except oxygen seems slightly underabundant, with $O/O_\odot = 0.7$–1.0, and iron is underabundant by $Fe/Fe_\odot = 0.5$–1.1 (see also Section 4.4). We find that the statistical errors on the abundances are large.

Table 4
The List of Recovered Emission Lines in the RGS1+2 Spectrum Obtained in Quiescence.

Ion	Line Center E_c (keV)–(Å)	$K_{\rm Gaussian}$ 10^{-5} (Phot. cm^{-2} s^{-1})	Flux 10^{-13} (erg cm^{-2} s^{-1})
C VI	$0.4577^{+0.0023}_{-0.0007}$–$27.088^{+0.04}_{-0.13}$	$1.9^{+1.3}_{-1.1}$	0.14
O VIII	$0.6520^{+0.0013}_{-0.0005}$–$19.015^{+0.015}_{-0.038}$	$3.6^{+0.8}_{-1.0}$	0.39
Fe XVII	$0.7574^{+0.0014}_{-0.0017}$–$16.370^{+0.036}_{-0.030}$	$0.9^{+0.6}_{-0.4}$	0.12
Fe XVII	$0.8261^{+0.0013}_{-0.0010}$–$15.008^{+0.009}_{-0.023}$	$0.50^{+0.30}_{-0.12}$	0.07
Fe XVIII/Fe XX	$0.8326^{+0.0009}_{-0.0014}$–$14.891^{+0.025}_{-0.016}$	$0.6^{+0.2}_{-0.3}$	0.08
Ne IX (f)	$0.9074^{+0.0019}_{-0.0035}$–$13.663^{+0.053}_{-0.028}$	$0.7^{+0.7}_{-0.4}$	0.10
Fe XX	$0.9694^{+0.0026}_{-0.0059}$–$12.789^{+0.079}_{-0.034}$	$0.6^{+0.2}_{-0.3}$	0.08
Fe XXI	$1.0065^{+0.0030}_{-0.0033}$–$12.318^{+0.037}_{-0.041}$	$0.6^{+0.2}_{-0.3}$	0.08
Ne X	$1.0206^{+0.0023}_{-0.0020}$–$12.148^{+0.024}_{-0.027}$	$1.0^{+0.6}_{-0.6}$	0.17
Fe XXII	$1.0516^{+0.0035}_{-0.0041}$–$11.790^{+0.046}_{-0.039}$	$0.6^{+0.5}_{-0.4}$	0.11
Fe XXIV	$1.1094^{+0.0031}_{-0.0095}$–$11.175^{+0.096}_{-0.031}$	$1.1^{+0.5}_{-0.5}$	0.20
Fe XIX/Ni XXIII	$1.1579^{+0.0107}_{-0.0064}$–$10.708^{+0.059}_{-0.097}$	$0.7^{+0.5}_{-0.5}$	0.13
Fe XVIII/Ne Xβ	$1.2053^{+0.0085}_{-0.0079}$–$10.287^{+0.067}_{-0.072}$	$0.40^{+0.30}_{-0.35}$	0.06
Fe XXI	$1.2993^{+0.0073}_{-0.0070}$–$9.542^{+0.051}_{-0.053}$	$0.5^{+0.3}_{-0.3}$	0.07
Mg XI (f)	$1.3319^{+0.0141}_{-0.0055}$–$9.308^{+0.038}_{-0.097}$	$0.40^{+0.25}_{-0.20}$	0.06
Mg XI (i)	$1.3484^{+0.0057}_{-0.0035}$–$9.195^{+0.024}_{-0.038}$	$0.9^{+0.3}_{-0.3}$	0.18
Fe XXIII	$1.3923^{+0.0004}_{-0.004}$–$8.907^{+0.022}_{-0.032}$	$0.6^{+0.3}_{-0.3}$	0.13
Mg XII	$1.4783^{+0.0084}_{-0.0111}$–$8.387^{+0.063}_{-0.047}$	$0.7^{+0.5}_{-0.4}$	0.16
Mg XII/Fe XXIII	$1.7525^{+0.0090}_{-0.0143}$–$7.074^{+0.058}_{-0.036}$	$1.2^{+0.6}_{-0.5}$	0.36
Si XIII (f)	$1.8410^{+0.0174}_{-0.0080}$–$6.735^{+0.029}_{-0.063}$	$1.3^{+0.6}_{-0.6}$	0.39
		Total Line Flux =	3.08

Note. Gaussian line fits are performed using coadded RGS1 and RGS2 data in the 0.4–2.2 keV range. A constant hydrogen column density of 0.18×10^{22} atoms cm^{-2} is used in the fits, in accordance with Table 1. $K_{\rm Gauss}$ is the normalization for the Gaussian line model. All lines are assumed to be narrow, as derived from the fits, where the line widths σ are constrained with the spectral resolution of RGS and taken to be fixed at 0.001 keV. All errors are calculated at the 90% confidence limit for a single parameter. Any upper limit is given at the 2σ significance level.

Table 5
The List of Recovered Emission Lines in the RGS1+2 Spectrum Obtained in Outburst

Ion	Line Center E_c (keV)–(Å)	$K_{\rm Gaussian}$ 10^{-5} (Phot. cm^{-2} s^{-1})	Flux 10^{-13} (erg s^{-1} cm^{-2})
Fe XXI/Ar XVI	$0.4952^{+\infty}_{-0.004}$–$25.037^{+0.023}_{-\infty}$	$0.55^{+0.62}_{-\infty}$	0.04
N VII	$0.5010^{+0.0005}_{-0.0010}$–$24.747^{+0.053}_{-0.021}$	$1.9^{+0.8}_{-0.8}$	0.15
O VII (f)	$0.5640^{+0.0011}_{-0.0025}$–$21.983^{+0.097}_{-0.042}$	$1.4^{+1.2}_{-1.1}$	0.12
O VII (i)	$0.5682^{+0.0003}_{-0.0006}$–$21.821^{+0.023}_{-0.011}$	$3.2^{+1.5}_{-1.5}$	0.27
O VII (r)	$0.5712^{+0.0016}_{-0.0017}$–$21.706^{+0.064}_{-0.060}$	$2.6^{+1.6}_{-1.6}$	0.23
O VIII	$0.6525^{+0.0005}_{-0.0004}$–$19.001^{+0.011}_{-0.014}$	$2.5^{+0.7}_{-0.6}$	0.28
O VIII	$0.6545^{+0.0013}_{-0.0005}$–$18.943^{+0.014}_{-0.037}$	$2.0^{+0.7}_{-0.9}$	0.21
Fe XVII	$0.7239^{+0.0009}_{-0.0006}$–$17.127^{+0.014}_{-0.021}$	$1.6^{+0.5}_{-0.6}$	0.18
Fe XVII	$0.7279^{+0.0008}_{-0.0010}$–$17.033^{+0.023}_{-0.019}$	$1.3^{+0.5}_{-0.5}$	0.15
Fe XVII	$0.7376^{+0.0017}_{-0.0004}$–$16.809^{+0.009}_{-0.038}$	$1.1^{+0.4}_{-0.4}$	0.13
Fe XVIII/O VIIIβ	$0.7710^{+0.0006}_{-0.0030}$–$16.081^{+0.062}_{-0.012}$	$0.55^{+0.30}_{-0.30}$	0.07
Fe XVIII	$0.7830^{+0.0043}_{-0.0043}$–$15.834^{+0.087}_{-0.086}$	$0.44^{+0.30}_{-\infty}$	0.06
Fe XVIII/Fe XX	$0.7930^{+0.0017}_{-0.0004}$–$15.635^{+0.008}_{-0.033}$	$0.33^{+0.30}_{-\infty}$	0.04
Fe XX/ Fe XIX	$0.8155^{+0.0004}_{-0.0012}$–$15.203^{+0.022}_{-0.007}$	$1.3^{+0.4}_{-0.4}$	0.16
Fe XVI/Fe XIX/Fe XX	$0.8237^{+0.0010}_{-0.0031}$–$15.052^{+0.056}_{-0.018}$	$0.75^{+0.40}_{-0.40}$	0.09
Fe XVII	$0.8266^{+0.0018}_{-0.0006}$–$14.999^{+0.023}_{-0.02}$	$0.8^{+0.4}_{-0.4}$	0.10
Fe XX/ Ne K$_\alpha$/Fe XVIII	$0.8600^{+0.0008}_{-0.0090}$–$14.417^{+0.15}_{-0.013}$	$0.5^{+0.3}_{-0.2}$	0.07
Fe XXI	$0.8860^{+0.0057}_{-0.0039}$–$13.994^{+0.06}_{-0.09}$	$0.4^{+0.3}_{-0.3}$	0.06
Ne IX (f)	0.9074 − 13.663 (fixed)	<0.37	<0.05
Ne IX (i)	$0.9160^{+0.0009}_{-0.0010}$–$13.535^{+0.014}_{-0.013}$	$1.0^{+0.6}_{-0.4}$	0.15
Ne IX (r)	$0.9290^{+0.0049}_{-0.0028}$–$13.335^{+0.040}_{-0.039}$	$0.5^{+0.4}_{-0.4}$	0.08
Ne X	$1.0198^{+0.0040}_{-0.0040}$–$12.157^{+0.048}_{-0.047}$	$0.6^{+0.4}_{-0.4}$	0.10
Fe XXII	$1.0603^{+0.02}_{-\infty}$–$11.693^{+0.224}_{-\infty}$	$0.2^{+0.4}_{-\infty}$	0.03
		Total Line Flux =	2.82

Note. Gaussian line fits and line fluxes performed using coadded RGS1 and RGS2 data in the 0.4–2.2 keV range. A constant hydrogen column density of 0.12×10^{22} atoms cm^{-2} is used in the fits, in accordance with Table 2. $K_{\rm Gauss}$ is the normalization for the Gaussian line model. All lines are assumed to be narrow, as derived from the fits, where the line widths σ are constrained with the spectral resolution of the RGS and taken to be fixed at 0.001 keV. All errors are calculated at the 90% confidence limit for a single parameter. All upper limits are given at the 2σ significance level.

4.4. Line Emissions in Quiescence and Outburst Revealed by RGS

For a better understanding of the characteristics of X-ray emission, we exploit the RGS spectra to detect lines that would reveal the state of the plasma independent of the continuum characteristics that would be dominant in the moderate-spectral-resolution EPIC data. We note here that the XMM-Newton RGS energy range is between 0.4 and 2.2 keV, which is smaller than the band for EPIC data (0.3–10.0 keV). Tables 4 and 5 list the detected lines for the RGS spectra in quiescence and outburst, respectively. For line identifications, the XSPEC task *identify* and the ATOMDB database (see Section 4.1) have been used. The calculations are made via fits with a Gaussian model to individual lines, or collections of two to three lines if there is blending, along with a power law for the base/continuum around the line feature. We have tabulated lines with photon fluxes $F_{\rm line} > 3 \times 10^{-6}$ phot. cm^{-2} s^{-1} ($>4 \times 10^{-15}$erg cm^{-2}s^{-1}). Tables 4 and 5 denote the line centers in kiloelectronvolts and angstroms, together with the photon fluxes of the lines as derived from the normalization of the fits and the corresponding energy flux. All errors are given at the 90% confidence limit for a single parameter. The detected lines and example fits to individual lines are displayed in Figures 7 and 8 for quiescence and outburst, respectively.

In the quiescent state, we detect all the Lα (H-like) lines of C (C VI), O (O VIII), Ne (Ne X), and Mg (Mg XII) that are in the energy range of the RGS. The strongest line is the H-like O VIII, with a flux of $(2.7–4.6) \times 10^{-14}$ erg cm^{-2} s^{-1}. In general, the He-like lines of metals (Ne IX, Mg XI, and Si XIII), except for C, which is not available, are recovered. None of the O VII lines (He-like oxygen) have been detected. RGS resolves the three components of the He-like lines that are forbidden, intercombination, and resonance line emissions. Among these, no resonance lines of any of the He-like triplets have been recovered along with no intercombination lines, except for Mg XI. All the forbidden emission lines of the triplets of Ne, Mg, and Si have been detected, with a range of energy fluxes $(0.6–3.9) \times 10^{-14}$ erg cm^{-2} s^{-1}. The rest of the detected emission lines are L-shell lines of iron from Fe XVII to Fe XXIII. The statistical quality does not allow the disentangling of some of the Fe lines. There may be blending or the spectral resolution is not high enough to tell some of the line emissions apart.

In the outburst state, we detect the H-like (Lα) lines N VII, O VIII, and Ne X, along with the He-like emission lines O (O VII) and Ne (Ne IX). The Lα emissions show a range of energy fluxes $(0.1–4.9) \times 10^{-14}$ erg cm^{-2} s^{-1}. The data quality (and the X-ray temperature) do not allow for detections above 1.1 keV. We do not detect Mg or Si lines. The detected H-like line fluxes (energy flux) of O and Ne are consistent with quiescent values, with some increase in O VIII and some decrease in Ne X. More importantly, this time the resonant emission lines of the He-like triplets are detected. They are

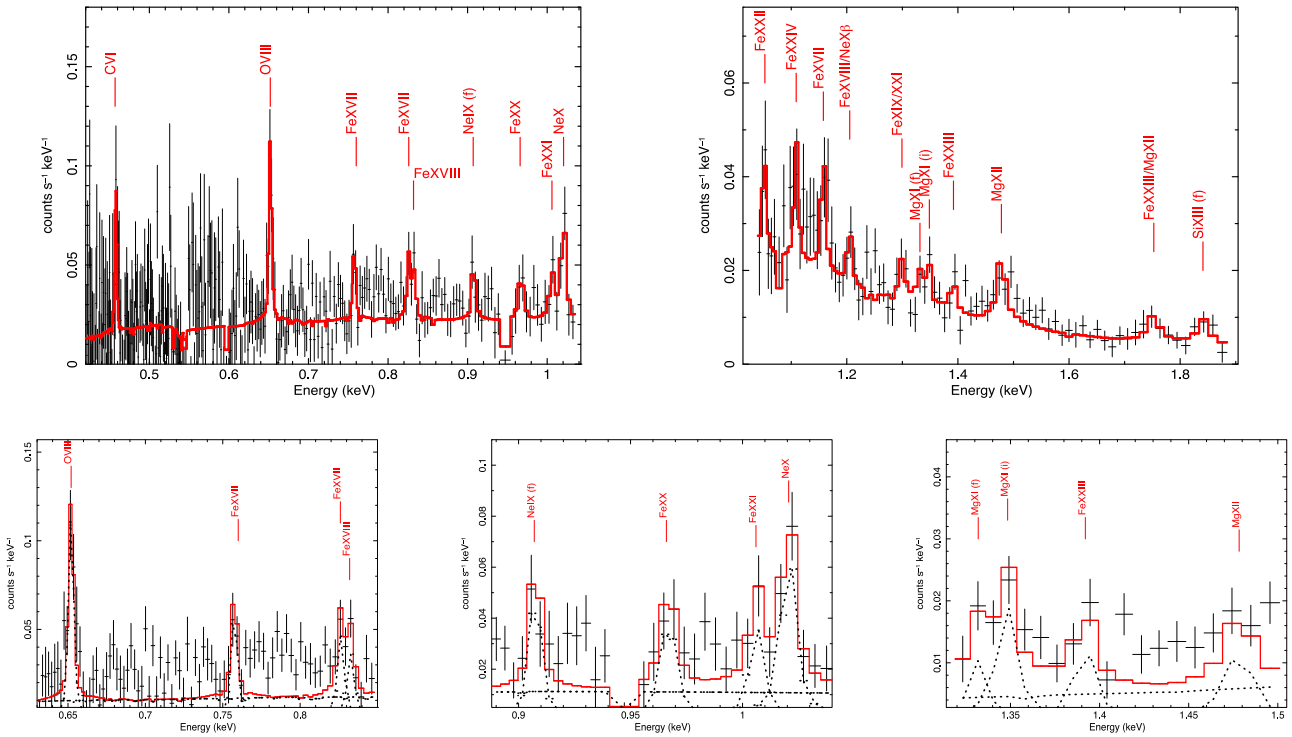

Figure 7. Averaged RGS 1+RGS 2 spectra of Z Cha in quiescence. The top panel shows identified lines labeled individually. The fitted high-resolution RGS spectrum is in the left panel of Figure 6. The three bottom panels show selected examples of fitted lines with a GAUSS emission model, as displayed in Table 4.

weak, but relatively stronger than the forbidden lines. The highest flux is in the intercombination lines of the triplets of O and Ne. The forbidden emission lines of O and Ne are detected in outburst, where the flux of Ne IX in outburst is half the flux in quiescence. No comparisons can be made for O VII. The energy flux of the forbidden line of oxygen (outburst) is about half the intercombination emission line of the triplet. O VIII (an H-like emission line) has similar fluxes in quiescence and outburst, only slightly higher in outburst. Several iron L-shell lines are detected between Fe XVII and Fe XXIII, with energy fluxes in a range $(0.3–1.8) \times 10^{-14}$ erg cm^{-2} s^{-1}, where the strongest emission is in Fe XVII.

In general, the total emission-line flux is similar in both quiescence and outburst, with $\sim 3 \times 10^{-13}$ erg cm^{-2} s^{-1}. We may not have resolved weaker emission lines (than the quoted upper limit) or lines outside the RGS range.

5. Discussion

5.1. Line Diagnosis and the Nature of the Accretion Flows in Z Cha

Collisional coronal plasma diagnosis utilizes line ratios that are sensitive to electron density and electronic temperature. Several processes are involved. Collisional excitation forms lines from the ground level with or without recombination. H-like radiative recombination can be important at high temperatures or, depending on the temperature and densities, He-like recombinations may even dominate. In general, at high temperatures (in the X-ray emission regime), the plasma can be dominated by collisional excitation or by radiative recombinations, revealing photoionized plasma. Hybrid plasmas show both characteristics where recombination and collisional processes occur. The ratios of H-like and He-like ions can be used for collisional plasma diagnostics. The He-like triplet comprises the resonance line (r: $1s^2\ ^1S_0$–$1s2p\ ^1P_1$), the intercombination line (i: $1s^2\ ^1S_0$–$1s2p\ ^3P_{2,1}$), and the forbidden line (f: $1s^2\ ^1S_0$–$1s2p\ ^3S_1$) emissions corresponding to transitions between $n = 2$ and the $n = 1$ ground-state shells. There are two particular ratios between these triplet line emissions: (1) the $R = f/i$, $R(n_e)$ ratio, yielding electron density diagnostics; and (2) $G = (f + i)/r$, which is a function of the electron temperature T_e. Large G ratios and a low resonance line indicate photoionization-(and radiative-recombination-) dominated plasmas, while $G < 4$ along with an intense resonance line is a signature of hybrid plasmas, where both collisional processes and photoionization are effective. At low G ratios, collisional excitation processes dominate. The G ratios can yield a good measure for electron temperature, but this ratio can vary by 2 orders of magnitude when the column density increases/changes (from 10^{17} to 10^{24} cm^{-2}; R. L. Porter & G. J. Ferland 2007). The R ratio is a good density probe. This ratio tends from high values at high f intensity to low values where intercombination lines are dominant. The low R ratios are indicative of high densities, so prominent forbidden lines signal low electron densities.

We have derived the R and G ratios using the O, Ne, and Mg triplets that have been detected for Z Cha. The R and G ratios using these triplets have also been calculated in E. M. Schlegel et al. (2014) for other accreting CVs. In quiescence, the triplets of Ne and Si show only the forbidden line emission, so no R or G ratios can be derived. Only Mg XI shows the forbidden and the intercombination line. We calculate that $R \simeq 0.44$. No resonance line is detected for any He-like triplet in quiescence. Therefore, no ratio of the H-like line to the resonance r line of the He-like triplet can be calculated. However, the same ratio is 1.4–1.7 using the forbidden lines, f, of neon and magnesium. In outburst, the

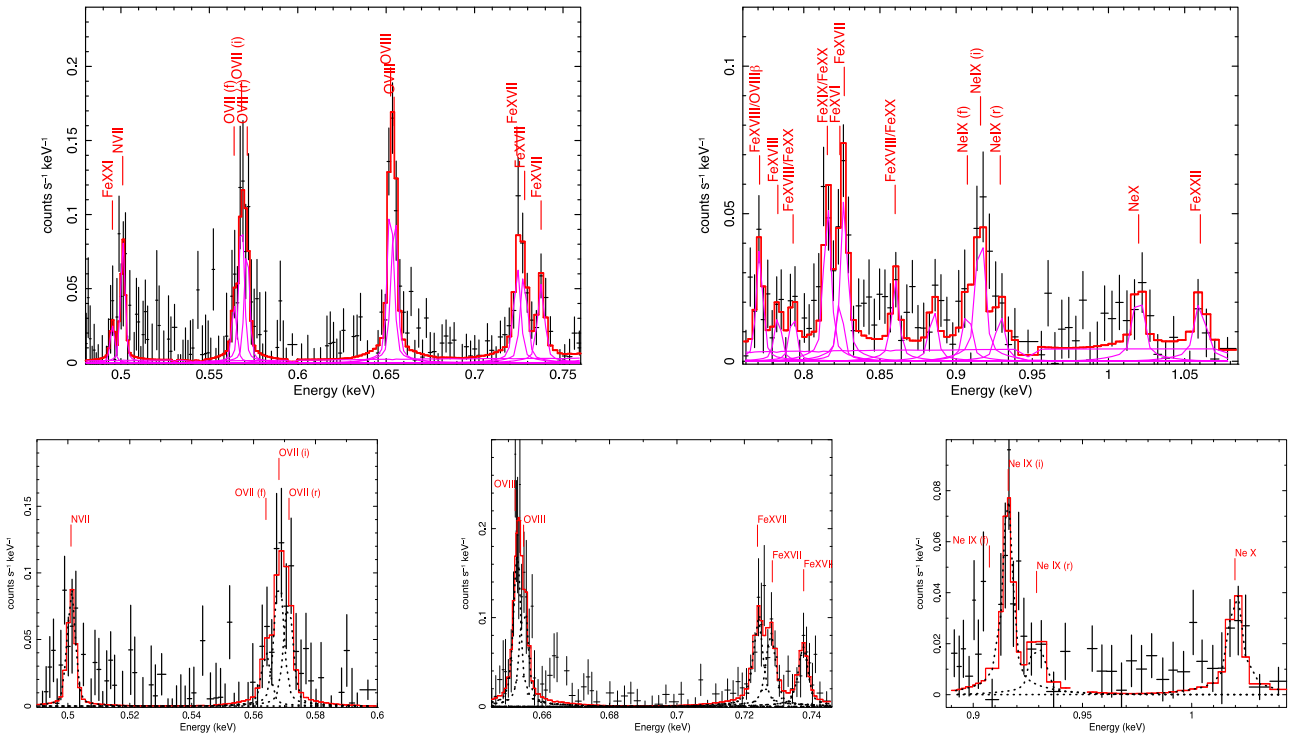

Figure 8. Averaged RGS 1+RGS 2 spectra of Z Cha in outburst. The top left and right panels show identified lines labeled individually. The fitted high-resolution RGS spectrum is in the right panel of Figure 6. The bottom three panels show selected examples of fitted lines with a GAUSS emission model, as displayed in Table 5.

He-like triplets of O and Ne are detected with the *f, i*, and *r* emission lines. For oxygen (O VII), $R \simeq 0.44$ and $G \simeq 1.8$. For neon, $R \simeq 0.4$ and $G \simeq 2.7$. The ratio of the H-like line to the resonance, *r*, line of the He-like triplet is ∼1 for both oxygen and neon. The same ratio is 1.7 using the forbidden lines (similar for both O and Ne), and the intercombination lines yield a ratio of 0.6–0.8 (the *i* line intensities are brighter). As a result, the low R ratios in outburst indicate higher densities compared to quiescence, with $n_e \simeq 7 \times 10^{11}\,\mathrm{cm}^{-3}$ for oxygen and $n_e \simeq 9 \times 10^{12}\,\mathrm{cm}^{-3}$ for neon, following from E. Silver et al. (2000). The *G* ratios of oxygen and neon are indicative of regions with $T_e \simeq (2\text{–}3) \times 10^6\,\mathrm{K}$, in accordance with D. Porquet & J. Dubau (2000). In quiescence, the nondetection of the *r* and *i* lines and the detection of *f* lines (except for Mg XI) indicate that the X-ray-emitting plasma has lower density compared to the outburst and the plasma is not collisional, most likely not in equilibrium, and is not photoionized much, either. The comparable forbidden line emission to the H-like species also supports this. This condition improves in outburst and most regions have higher densities and more collisional processes (i.e., collisional excitation), owing to the *r* lines. However, prominent *i* lines compared with even the H-like species indicate photoionization is appreciable (i.e., recombination), and thus the X-ray-emitting plasma may be "hybrid." However, the relatively low flux in the resonance lines compared to the intercombination and H-like lines indicates that a full collisional ionization equilibrium is not set in the plasma, even in outburst.

The iron L-shell lines can also be used as density and electron temperature probes. We have detected some of these lines securely in the outburst RGS data. The ratio of Fe XVII lines at 0.81–0.82 keV (15.01–15.26 Å) is correlated with electron temperature (G. V. Brown et al. 2001; E. M. Schlegel et al. 2014; for CVs). The lines at 15.01 Å and 15.26 Å are also known as 3C resonance and 3D intercombination lines, respectively. The entire set of Fe XVII 3s/3d (0.72–0.82 keV) defines a temperature measure with intensity ratio $I\,(16.77 + 17.05 + 17.10\,\text{Å})/\ I\,(15.01 + 15.26 + 15.45\,\text{Å})$ (G.-X. Chen & A. K. Pradhan 2005). This ratio is about 1.4 (assuming we have not recovered the 15.45 Å line). This yields an electron temperature of $T \sim 6 \times 10^6$ K, consistent with the RGS spectral results. The ratios of Fe XVII lines—which are 17.01/16.77 Å and 17.10/17.05 Å, are calculated in a range (1.2–1.5) yielding electron densities $<10^{13}\,\mathrm{cm}^{-3}$. E. M. Schlegel et al. (2014) show the dependence of the ratio on densities (for CVs) and related references. Our densities are in accordance with those calculated using these triplet lines.

A more fundamental characteristic of a plasma is the ionization balance. The line spectrum is sensitive to deviations from ionization equilibrium. A Bremsstrahlung continuum immediately follows the changing plasma conditions, so that the line-to-continuum ratio indicates deviations from equilibrium (note that significant abundance changes can also affect the line-to-continuum ratio). Typically, a plasma will reach CIE conditions when $n_e t \sim$ several $\times\, 10^{13}\,\mathrm{s\,cm}^{-3}$ (i.e., the ionization parameter). For most atoms, equilibrium may be achieved by a factor of 10 earlier, depending on electron density and plasma temperature, where light atoms (e.g., C and O) may achieve equilibrium even earlier. At low *T* ($<10^6$ K), L-shell ions dominate, and at high *T*, the ion population is dominated by He-like, H-like, or bare ions (see R. K. Smith & J. P. Hughes 2010). For iron to reach ionization equilibrium, an ionization parameter of several $\times 10^{12}\,\mathrm{s\,cm}^{-3}$ may be sufficient. Given these characteristics and the derived values of ionization parameters for Z Cha, spectral results reveal plasma that is near ionization equilibrium but not in equilibrium (see the discussion in the next section).

5.2. Comparison of Quiescence and Outburst in X-Rays

An overall elaboration of the quiescence and outburst spectral analyses is necessary to understand the accretion flow characteristics in the Z Cha system. Comparative studies of DNe in quiescence and outburst constitute an essential tool for understanding accretion physics in CVs and related objects and DIM phenomena. The outburst EPIC light curve yields only a 13% pulsed fraction at the orbital period of Z Cha, which is 1.788 hr (see Section 3) and lies below the period gap. In quiescence, the source shows deep eclipses in the optical and the X-ray light curve indicates nondetections on a similar timescale to the eclipse durations of 319–329 s given by A. A. Nucita et al. (2011), which indicates very large modulation depths. These modulation discrepancies (outburst and quiescence) show that the X-ray-emitting region is definitely extended during outburst, which is a characteristic of hot accretion flows in the X-rays. The nondetection in quiescence can be due to occultation or rather absorption in the system of fully/partially covering cold or ionized absorbers intrinsic to the system. This is also revealed in the mean light curves in the *B* band and the X-rays during outburst, where the former show very narrow deep dips and the latter show a wider depression of the pulse profile over 0.3 phases, which is about one-third of the orbit (at the least).

For the analysis in quiescence, we used CEVMKL or the nonequilibrium ionization plasma model, VNEI, in XSPEC for the continuum and line modeling (see the descriptions in Section 4.1). Table 1 shows six different fits using these plasma models along with different absorber models. The χ^2_ν of the fits indicate not much difference between the CEVMKL model that indicates CIE and the nonequilibrium ionization model VNEI. The plasma temperatures are a kT of 5.4–8.6 keV with the VNEI model and $kT_{\rm max} = 7.2$–13.0 keV for the CEVMKL model fits, with a source luminosity of $(5.0$–$6.0) \times 10^{30}$ erg s^{-1} using both plasma models. The lower limits on the temperatures represent values where a power law is added to the composite spectral model, which yields a photon index of index of 1.2–1.5 at a nonthermal luminosity of $(1.4$–$3.0) \times 10^{30}$ erg s^{-1}. The power-law component statistically improves the fits, but they are not any better than when a complex absorber model is applied to the spectrum. The spectral fits yield better χ^2_ν values when using partially covering absorbers as opposed to the *tbabs* absorber model. A partially ionized absorber model, *zxipcf*, gives an equivalent $N_{\rm H} = (3.4$–$5.9) \times 10^{22}$ cm^{-2} and a $\log(\xi) = 3.5$–3.7 with a (50–60)% covering fraction when the VNEI model is used. A CEVMKL plasma model yields an equivalent $N_H = (9.4$–$11.0) \times 10^{22}$ cm^{-2} and a $\log(\xi) = 1.81$–1.95 with a (35–37)% covering fraction. These values are 40–80 times more than the hydrogen column density of a cold partially covering absorber with $N_{\rm H} = (0.11$–$0.19) \times 10^{22}$ cm^{-2} that is consistent with all plasma models and the interstellar absorption toward the system. Finally, the quiescent spectrum also shows the Fe XXVI absorption line at 6.95 ± 0.05 keV detected for the first time in a DN with line $\sigma = 0.05$–0.10 and depth in a range 0.04–0.16. The optical depth at the line center follows from the line depth parameter as 0.32–0.65, which indicates an optically thin absorbing medium. Such iron absorption lines are indicators of warm absorbers in X-ray binaries (Ş. Balman 2009; M. Díaz Trigo & L. Boirin 2016). We find that the partially covering ionized absorber that we use with the VNEI plasma model is consistent with this absorption-line detection. In general, the CEVMKL model finds a colder ionized absorber with higher equivalent hydrogen absorption by a factor of 3–5.

The line diagnosis of quiescent RGS data shows no resonance lines of the He-like O, Ne, Mg, Si, or N. Only the forbidden lines of Ne, Mg, and Si exist together with the H-like C, O, Ne, and Mg. The strongest line is O VIII, with $(2.7$–$4.6) \times 10^{-14}$ erg s^{-1} cm^{-2}. The forbidden-line-emitting He-like lines of Ne and Mg have fluxes of $(0.6$–$3.9) \times 10^{-14}$ erg cm^{-2} s^{-1}, which is only a factor of 1.4–1.7 times less than the H-like line fluxes (of the same species). The quiescent X-ray-emitting plasma, therefore, is not collisional, lacking the resonance lines of all the He-like species, and not in ionization equilibrium, as the line diagnosis indicates (see Section 5.1). Note that EPIC reveals an ionization timescale of $(2.8$–$6.0) \times 10^{11}$ s cm^{-3} (consistent with the RGS result), indicating that plasma is near to but not in ionization equilibrium (see also D. A. Liedahl 1999; R. K. Smith & J. P. Hughes 2010). This nonequilibrium ionization condition in quiescence is consistent with the nature of the ADAF-like hot advective accretion flows. Moreover, the broadband noise structure and the band-limited noise (BLN; $f_{\rm break} = 1.0 \pm 0.4$ mHz) detected in this system, together with the X-ray lags (i.e., lagging UV) of 112–209 s (Ş. Balman 2020), all support the ADAF-like hot advective accretion flows in the inner disk during quiescence.

During outburst, the EPIC data yield a plasma temperature of $kT_{\rm max} = 0.97$–3.20 keV at a luminosity of $(1.4$–$2.5) \times 10^{30}$ erg s^{-1}, where the temperatures are much lower compared to quiescence, along with a diminished X-ray luminosity. A CEVMKL model of plasma is used in all four fits displayed in Table 2, since a VNEI plasma model did not yield an acceptable χ^2_ν below 2, because it did not fit the iron line between 6 and 7 keV properly. The α parameter, which is the power-law index of the distribution of plasma temperatures for the CEVMKL model, is found to be <0.1 with best-fit results $\sim$0.01, which is the value recovered for the NL systems (Ş. Balman et al. 2022), consistent with the high-state nature of Z Cha in outburst. There is more complex absorption in the system during the outburst, where one of the cold partially covering absorber components is similar to the one in quiescence and the second one is larger by a factor of 15, $(8.7$–$10.7) \times 10^{22}$ cm^{-2}. On the other hand, the outburst EPIC spectra are also consistent with a partially ionized absorber model, *zxipcf*, which shows a very large equivalent $N_{\rm H} = (2.30$–$2.95) \times 10^{24}$ cm^{-2}, with an ionization parameter $\log(\xi)$ in a range 2.79–2.83 (the covering fraction is 90%), which is about a factor of 25–50 times more than the quiescence value. This is the only fit with the CEVMKL model where the He-like weak iron line is correctly attributed by the plasma emission model (no need for an additional GAUSS model). However, this amount of partially ionized absorption is physically not consistent with observations of DNe (K. Mukai 2017; Ş. Balman 2020). Outburst spectral modeling allows for a blackbody model or a power-law model assumed together with CEVMKL plasma emission. This gives a plasma temperature $\sim$1 keV, and an additional iron line at $6.64^{+0.06}_{-0.07}$ keV is necessary to yield acceptable fits. The blackbody model at 0.021–0.035 keV is significant at only the 93% confidence level (slightly less than 2σ). The blackbody luminosity is 3.4–0.7×10^{31} erg s^{-1} (unabsorbed, 0.1–10 keV), which is several orders of magnitude less than SAD model expectations at high states (also below the expectations of

DIM). This value of luminosity is about only ∼20 times less than the bolometric blackbody luminosity at this temperature. A power-law model along with CEVMKL without a blackbody models the EPIC spectra well, with a similar χ^2_ν along with an additional He-like iron line. The associated power-law photon index is 1.5–1.7 at a luminosity of $(3.0–3.9)\times10^{29}$ erg s^{-1}, similar to NLs but with a lower luminosity (Ş. Balman et al. 2022; see also Ş. Balman 2015); A. Dobrotka et al. 2023).

The outburst line diagnosis shows He-like O and Ne, with intercombination lines being the strongest, along with weaker resonance lines. The R ratios in outburst show electron densities $(7–90)\times10^{11}$ cm^{-3}, calculated from the O and Ne lines, and the G ratios yield electron temperatures of $(2–3)\times10^6$ K. These indicate that the plasma is more collisional (resonance lines exist) and denser than in quiescence, but not yet in a full CIE, as the RGS data indicate ionization timescales of $(0.97–1.40)\times10^{11}$ s cm^{-3} (less than quiescence by two to six times). All detected lines are narrow, limited by the resolution of RGS, yielding Keplerian rotational velocities <1000 km s^{-1}, which is low for any BL and consistent with the nature of extended advective hot flows at sub-Keplerian speeds. The flow is most likely not homogeneous, but patchy with higher- and lower-density regions. In outburst, the accretion flow (partially ionized) is denser by a factor of ∼60 compared to quiescence, calculated using the ratio of ionization parameters (i.e., under the assumption of similar ionizing X-ray luminosity and a similar location; $\xi = L/(nr^2)$). Overall, the X-ray emission from Z Cha shows ADAF-like advective hot-flow characteristics in quiescence and outburst.

5.2.1. A Closer Look Into the Comparison of EPIC and RGS Spectra

There are two handicaps in the spectral analysis of Z Cha in quiescence and outburst. The first is the very high equivalent $N_{\rm H}$ of the partially ionized absorption attained in the outburst using EPIC data (only, but not with RGS). For this matter, in place of *zxipcf* (an old version of the *warmabs* model for partially ionized absorption), we utilized the XSTAR warm absorber model *warmabs,*[17] which is a multiplicative local model that can be incorporated into any XSPEC distribution for spectral analysis. The model is a collection of warm absorption and photoionized emission models derived from the XSTAR program that calculates the physical conditions and spectra of photoionized gases. We used *warmabs* as a substitute for *zxipcf* in QFit-5, which uses the VNEI model (see Table 1) for quiescence and OFit-3 in outburst. The fit for quiescence yields the same χ^2_ν for dof of 1399 (there is no covering fraction parameter; it is 1.0). The equivalent $N_{\rm H} = (0.5–0.7)\times10^{22}$ cm^{-2} with $\log(\xi) = 3.09–3.17$. The ionization parameter is similar but the equivalent $N_{\rm H}$ is about 10 times less than measured by *zxipcf*. We applied the same replacement in OFit-3 for the outburst, using a CEVMKL model. We obtained $N_{\rm H} = (0.020–0.009)\times10^{22}$ cm^{-2} with $\log(\xi) = 1.33^{+0.80}_{-0.80}$. The $\chi^2_\nu = 1.38$ for dof of 459. This is not as good as OFit-3, where $\chi^2_\nu = 1.24$ for dof of 450, but it is quite acceptable. The discrepancy in the equivalent $N_{\rm H}$ parameter between outburst and quiescence is about 30–50, but with more physically relevant equivalent $N_{\rm H}$ values in outburst. Therefore, the equivalent $N_{\rm H}$ for the partially ionized absorption model in Table 2 should be taken with caution. Moreover, the ionization parameter for the warm absorber in outburst is different and lower (determined by the *warmabs* fit), indicating a colder absorber. Note here that the line diagnosis with RGS finds nonequilibrium plasma in quiescence, but the EPIC spectra can be modeled well by both NEI and CEI models.

The RGS finds similar results to EPIC in quiescence, but a factor of 5 times less equivalent $N_{\rm H}$ for the *zxipcf* model; all RGS results are similar to the results of the *warmabs* fit for EPIC. In the outburst, the RGS fits have a similar ionization parameter to the *zxipcf* absorber model for EPIC, but have a factor of 90 times less equivalent $N_{\rm H}$ than the *zxipcf* model. Compared with the *warmabs* model fit of EPIC, the equivalent N_H determined by RGS is only about 10 times more, but the ionization parameter is still different and lower, indicating a colder absorber in the *warmabs* fit for EPIC. We note here that for a successful fit with RGS using a *zxipcf* model, only the VNEI plasma code gives fits with acceptable χ^2_ν values under 2. This is consistent with the line diagnosis but not with EPIC fits.

The second handicap follows from the fits in the above paragraph and the fact that for the outburst EPIC spectra, the VNEI model fits do not yield any acceptable χ^2_ν, because the He-like iron line cannot be fitted by this plasma emission model. For spectral fits with EPIC, the CEVMKL plasma model is assumed for the outburst. Note here that line diagnosis by RGS, as noted above, shows that the X-ray-emitting plasma is not in the CIE state in both phases of the source. The outburst RGS spectra can be reasonably well modeled with the nonequilibrium ionization plasma model, VNEI. To account for this dichotomy, we have applied a composite model of a complex absorber and two plasma emission models, CEVMKL and VNEI, simultaneously fitted to the EPIC spectra. The resulting fit had $\chi^2_\nu = 1.29$ (dof = 444), which is not the best-fitting model but is the best-fitting physical model. The complex absorber had two components: (1) a partially covering cold absorber; and (2) a partially covering ionized absorber (warm absorber). The cold absorber was similar to the fitted interstellar absorption in quiescence or outburst. The warm absorption was $N_{\rm H} = 1.6\times10^{23}$ cm^{-2} with $\log(\xi) = 1.08$ and a covering fraction of 80%. This is less than the value in Table 2 by factor of 16. This corrects the overpredicted ionized absorption in the EPIC data during outburst. The ionization parameter is much lower, depicting a significantly colder warm absorption in outburst (consistent with the *warmabs* fit in the first paragraph of this subsection). The plasma model parameters in Table 2 (for CEVMKL) and in Table 3 (for VNEI) are very similar to this two-plasma model fit. Particularly, we were able to recover the same temperatures as displayed in the different tables (OFit-3 and Outburst-2), which makes the EPIC and RGS results consistent. The normalizations and ionization timescales hold within a factor of 2 (OFit-3 and Outburst-2). Therefore, we suggest that the X-ray emission region in the outburst indicates local NEI and CIE conditions that would maintain the EPIC and RGS consistency in outburst.

5.3. The DN State Transition of Z Cha and the Disk Outburst Phenomena

5.3.1. The State Transition in the Optical and UV

In order to fully understand the X-ray evolution of the DN Z Cha through state transitions, we need to peek at the UV and

[17] https://heasarc.gsfc.nasa.gov/xstar/docs/html/node102.html; the latest version—2.47—is used, which involves a better atomic database, level populations, lines, rrc opacities, and line emissivities.

the optical wavelength characteristics of these transitions. During peak outburst, the accretion disk dominates the UV light curve of Z Cha, with a mass accretion rate of the order $1 \times 10^{-9} M_{\odot}\,\mathrm{yr}^{-1}$. This value of accretion rate amounts to a disk luminosity $\sim 5 \times 10^{33}\,\mathrm{erg\,s}^{-1}$, given a WD mass of $0.7 M_{\odot}$ and a radius of 7.7×10^{8} cm. In the UV and optical, the disk seems to remain optically thick for two weeks after outburst. The WD temperature after outburst is about 20,000 K and declines to 15,700 K in quiescence, with the bright spot (the region where the stream impacts the edge of the disk) being hotter, around 16,700 K. By the third week, the disk is optically thin in the UV (see E. L. Robinson et al. 1995). The bright spot appears to be a non-negligible emitting component in the system, and it is a source contributing to the flickering light of Z Cha during quiescence (A. Bruch 1996), indicating it is a rather active region.

UV and optical observations of Z Cha during quiescence reveal a continuum slope of -1.7 (in log units) over an orbital period/phase, which is much flatter than the expected -3.5 (or so) for an accretion disk (M. W. Rayne & J. A. J. Whelan 1981). The main reason for this discrepancy is the high inclination of the system, where the disk is seen nearly edge-on. Furthermore, it has been shown (J. Smak 2012) that in quiescence, the stream material at L1 overflows the edge of the disk in a manner similar to the eclipsing system OY Car, which is known to be heavily veiled in the UV (K. Horne et al. 1994). This explains the need for an ionized warm absorber (in addition to the interstellar medium (ISM) component) in our modeling of the X-ray data during quiescence and could be responsible for the more complex nature of the absorption components. In fact, in a number of CV systems, the WD appears to be masked by the L1 stream material overflowing the disk edge, severely affecting the continuum flux level (P. Godon 2019), especially for higher-inclination systems near orbital phase 0.75 ± 0.10 and even near 0.25 ± 0.10. Stream overflow is expected to occur more easily for quiescent DNe (F. V. Hessman 1999), but in outburst the disk in Z Cha becomes flared (E. L. Robinson et al. 1999), and it is likely that the disk edge occults to some extent the inner part of the disk and the WD. For example, EM Cyg (with an inclination of 67°) in outburst exhibits a disk UV flux and slope decreasing dramatically near orbital phase 0.75, where the stream overflows the disk (P. Godon 2019, Figures 1 and 2, bottom left), due to both an inflated disk edge and stream material flowing over the disk. For a high-inclination eclipsing system like Z Cha, the flared disk in outburst is likely veiling the inner disk and WD at all orbital phases. This could explain the warm absorber being 30–50 times larger in outburst than in quiescence and the need for a cold absorber, too.

The spectrum of the secondary in Z Cha is contaminated by the accretion disk, making proper identification of its spectral type uncertain. Assuming an M5 classification, R. T. Hamilton et al. (2011) find the CO features (in the IR) much weaker than they should be, indicating the possibility that the secondary (and therefore the accretion disk) might be deficient in C (CNO-processed?). While here we find some agreement with solar abundances, the underabundance of oxygen we find is consistent with weaker CO features.

5.3.2. The State Transition in the Context of Compact X-Ray Binaries

Black hole (BH) and neutron star (NS) low-mass X-ray binaries (LMXBs) spend most of their time in a quiescent state and exhibit disk outbursts in the theoretical framework of DIM, where they increase in emissivity, in luminosity, and go through distinct spectral states during outbursts (R. A. Remillard & J. E. McClintock 2006; T. M. Belloni et al. 2011), where the timescales of occurrence and durations are not very similar to DNe (i.e., longer). In addition, some turn out to be failed outbursts (M. Del Santo et al. 2016). Timing properties (e.g., noise characteristics) also change dramatically between states. For some quasi periodic oscillations (QPOs), some time lags and BLN resemble the ones detected for CVs and DNe (see Ş. Balman 2019 for a review and comparisons), where the broadband noise structure in the optically thick disk decreases in strength in outburst, while the noise moves to higher frequencies and gets more coherent (e.g., the appearance of QPOs; Ş. Balman et al. 2022). LMXB transients are believed to move in a counterclockwise fashion through a q-diagram (in hard- and soft-color space or luminosity versus spectral color space), as they change from a quiescent and hard state (a hot-flow and jet-dominated state) to a soft high state (with disk winds) that is disk-dominated, then finally back to quiescence. A few DNe do show this behavior, where a soft-X-ray blackbody-emitting BL (e.g., SS Cyg; E. Körding et al. 2008) is observed with a detection of nonthermal synchrotron emission, interpreted as jet formation. Not all DNe show such behavior (see Section 1.1), where mostly the hard X-ray emission in quiescence diminishes in flux and temperature, gets softer in the outburst, then recovers back to the quiescent higher fluxes and temperatures. This requires a clockwise rotation as opposed to counterclockwise rotation on a q-diagram. The physical explanation of this is beyond the scope of this paper, but we believe it resides in the ADAF-like structures that form in the inner disks that persist throughout a DN outburst, as detected and studied for Z Cha in this paper. This is different than the standard LMXB picture. DNe and CVs, in general, aside from supersoft X-ray sources, are not very bright in accretion luminosity.

NSs, as opposed to BHs, have a hard surface encountered by the accretion flow, where shocks and BLs are observed. NS LMXBs also show cooler coronae than BH LMXBs, cooled perhaps by the extra source of soft photons from the NS or the inner disk. BH and NS LMXBs indicate a strong power-law component that evolves throughout the outburst, from flatter photon indices in hard and intermediate states to steeper ones ($\Gamma > 2.1$) in soft states. This component is connected to the hot coronal flows and jet emissions in these systems (unless it is from the NS itself; e.g., millisecond pulsars). High-state CVs, DNe, and, as in this work, Z Cha show a power-law component in the outburst state at photon indices similar to LMXB transients, provided that soft high states in the X-rays (blackbody-emitting disks) are rarely encountered, thus the photon indices remain flatter. Note that some of our spectral fits for Z Cha with equally acceptable χ^2_{ν} do not require a power-law model in quiescence or outburst. For LMXB transients, jets, winds, and accretion states are well studied, where jets dominate hard states and winds are stronger in the soft states with 200–3000 $\mathrm{km\,s}^{-1}$, where such winds exhibit warm absorber effects on the emission internal to the absorbing regions or the central source (R. P. Fender et al. 2004; J. M. Miller et al. 2008; J. Neilsen & J. C. Lee 2009; G. Ponti et al. 2012; M. Díaz Trigo & L. Boirin 2016). For high-state CVs and DNe in outburst, we observe similar effects of warm absorbers (i.e., derived from spectral fits), most likely as a

result of disk wind formation in the outburst phases, as described for Z Cha. Furthermore, we detect warm absorber effects, also in quiescence, similar to, e.g., LMXB dippers (Ş. Balman 2009 and references therein). Jet formation (during outbursts) is suggested for DNe with radio detections of a handful of systems at the onset of outburst (D. L. Coppejans & C. Knigge 2020), but weak detections hinder any further study.

The general characteristics of ADAF-like flows and disk geometry are described, also in the context of CVs, in Ş. Balman (2020) and Ş. Balman et al. (2022) and will not be repeated here. In general, the accretion flow and the disk structure in X-ray binaries can be described as an interplay between an outer SAD and an inner ADAF, which is responsible for the ejection of the jets (JED: jet-emitting disk), along with an accretion-disk corona found to co-exist with this dichotomic structure (R. Narayan & I. Yi 1994; A. A. Esin et al. 1997; F. Yuan & R. Narayan 2014). This JED–SAD hybrid disk provides a successful explanation that describes the state transitions and also matches the evolution of QPO structures detected in LMXB transients (J. Ferreira 1997; G. Marcel et al. 2019, 2020). This type of hybrid structure is also described as forming a torus (e.g., non-self-gravitating axisymmetric thick tori in NS LMXBs) in the central regions of these transients, where the radial and vertical oscillations of this torus structure are used to describe the QPOs (e.g., kilohertz QPOs) in LMXBs (L. Rezzolla et al. 2003; V. Parthasarathy et al. 2017; M. G. B. de Avellar et al. 2018). Such a torus or the inner advective (ADAF-like) hot flow region is believed to be large (i.e., size) in hard states, where the optically thick disk is more distant and the torus or inner advective hot flow can expand. There is likely a small/er torus or inner advective/coronal structure in soft states when the inner disk is compressed as a result of the increased accretion rate. This prescription is in accordance with spectroscopic results for Z Cha, since we find that the X-ray-emitting region is denser and cooler in outburst, thus smaller than that in quiescence, where the X-ray temperature is about 10 times more, with lower densities, as the flow is not very collisional and the forbidden lines of He-like elements persist (with no intercombination and resonance lines), so the geometry is larger than the outburst. Note here that the break frequency for Z Cha (1.0 ± 0.4 mHz) in quiescence indicates transition (e.g., into an advective hot flow) around 1.5×10^{10} cm (using $\nu_0 = 1/2\pi (GM_{\rm WD}/R_{\rm in}^3)^{1/2}$). The brightness temperature measurements in quiescence (optical) imply a deviation from the standard structure around $0.5R_{\rm L1}$, where $R_{\rm L1}$ (the distance between the inner Lagrangian point and the WD) is calculated to be 3.0×10^{10} cm (J. H. Wood 1990), which makes our disk structure model for Z Cha consistent across wavelengths.

6. Conclusions

Comparative studies of DNe in quiescence and outburst constitute an essential tool for understanding accretion physics in CVs and related objects. Z Cha, being a close-by eclipsing SU UMa–type DN below the period gap, has been studied over most of the electromagnetic spectrum in quiescence and outburst. In this paper, we have presented X-ray spectroscopy of Z Cha using the EPIC and RGS instruments of the XMM-Newton observatory (i.e., an archival study). Such data are scarce and worthwhile for an in-depth and detailed study for drawing information on state transitions of DNe and CVs though disk outbursts. Our main aim was to do rigorous spectral modeling to understand the conditions in the X-ray-emitting plasma during quiescence and how that changed in the outburst.

Our results are consistent with the general observational picture, where the (hard) X-ray luminosities and temperatures are higher in quiescence, and a hard-X-ray-emitting plasma always remains in outburst. A soft-X-ray blackbody emission is found as part of a composite spectral fit to the outburst data, but is not significant enough to be the best-fitted model and the soft-X-ray luminosity was about 1000 times below the SAD and DIM theory expectations for a mass accretion rate of $10^{-9} M_\odot\,{\rm yr}^{-1}$. The quiescent hard-X-ray emission can be modeled by CIE (CEVMKL in XSPEC) or nonequilibrium plasma models (VNEI in XSPEC), yielding a kT of 5.4–8.6 keV with the VNEI model and $kT_{\rm max} = 7.2$–13.0 keV (with CEVMKL), where the lower limits come from composite fits, including a power-law model of emission. The spectra yield better χ^2_ν values using partially covering absorbers of a cold and photoionized nature. This is in accordance with the observations in the optical and UV, where stream overflow (and also hotspot region) and winds in the outburst are detected. The ionized absorber has an equivalent $N_{\rm H} = (0.5$–$0.7) \times 10^{22}\,{\rm cm}^{-2}$ with $\log(\xi) = 3.09$–3.17 when the *warmabs* model is used (along with VNEI, which has $\tau = 5.4 \times 10^{11}\,{\rm s\,cm}^{-3}$). Moreover, we find that in quiescence, at two different phases over the orbit (0.3 and 0.75), the warm absorber characteristics change and either the equivalent $N_{\rm H}$ is larger (a less pronounced dip in the light curve) or the warm absorber is colder and less ionized (a relatively deeper dip), similar to LMXB dipper characteristics. The first dip near phase 0.75 is due to the L1 stream material overflowing the disk edge, near phase 0.9, and directly veiling the inner disk (e.g., X-ray-emitting region) and the WD near phase 0.75 as it moves inward. The overflowing material is the most likely origin of the varying warm and cold absorption in the X-rays. In its ballistic trajectory, the stream material continues and hits the disk surface near phase 0.50 (T. R. Marsh 1986; S. H. Lubow 1989), where it bounces off the disk surface outward and veils the inner disk and the WD a second time, near phase 0.30, thereby causing a second dip (P. Godon 2019) as we view the warm absorption by this material in the X-rays. In the outburst, the flaring of the disk viewed at an angle above 80° is likely responsible for much of the complex phase-average X-ray absorption; particularly around phase 0.9, the L1 stream impacts the disk edge, thereby increasing its vertical extent, and we detect orbital modulation of the X-rays dipping between phases 0.7 and 1.0 as a result of the inferred absorption characteristics.

The line diagnosis in quiescence shows no resonance lines of the He-like O, Ne, Mg, Si, and N. Only forbidden lines of Ne, Mg, and Si are detected, together with the H-like C, O, Ne, and Mg. The strongest line is O VIII. The quiescent X-ray-emitting plasma is not collisional and not in ionization equilibrium, as the line diagnosis indicates, which is consistent with hot advective accretion flows in nature. The quiescent spectrum also indicates an Fe XXVI absorption line detected at 6.95 ± 0.05 keV for the first time in a DN using CIE plasma models, and when a nonequilibrium ionization model is used, the line detection is only 1.5σ–2σ, due to the weakness of the H-like Fe. The line diagnosis of the outburst RGS spectrum shows He-like O and Ne, with intercombination lines being the strongest, along with relatively weaker resonance lines, indicating electron densities $(7$–$90) \times 10^{11}\,{\rm cm}^{-3}$ (using R ratios). The fits yield electron temperatures 0.5–0.7 keV using

the VNEI plasma model. The X-ray plasma as seen by RGS is more collisional and denser in the outburst, but not in ionization equilibrium, with ionization timescales of $(0.97–1.4) \times 10^{11}$ s cm^{-3}. The EPIC data indicate that there is a dichotomy in the X-ray plasma in the outburst. The best-fitting physical model consistent with both RGS and EPIC spectra is a combination of the CEVMKL+VNEI models, where the lower temperatures are consistent with the NEI characteristics and, thus, the RGS spectrum. The higher energies and the higher plasma temperatures are consistent with a CIE model around ∼3 keV. In general, the X-ray-emitting region is extended and inhomogeneous, with perhaps higher- and lower-density regions. The radiative efficiency of the X-ray region is about 0.0004, comparing the disk and X-ray luminosities of the source in outburst. All the detected lines are narrow, with Keplerian rotational velocities <1000 km s^{-1} (outburst or quiescence), consistent with the advective hot-flow characteristics.

We can list the basic observational characteristics of advective hot flows in the X-rays for DNe (and CVs) as low emission efficiencies 0.01–0.0001, sub-Keplerian flows of nonionization equilibrium plasma with extended nonoptically thick disk structure (some power-law emission in high states), a BLN noise with break frequencies indicating a transition radius in a hybrid disk, and propagation lags (as in X-rays lagging the UV/optical). Overall, the X-ray emission from Z Cha shows ADAF-like advective hot-flow characteristics in quiescence and outburst. Our results have implications for all state transitions and disk outbursts, together with the accretion physics of high-state CVs (NLs) and accreting WDs. This work will help to improve theoretical studies of disk modeling, MHD formalism, and shock formation and outflows. Our study also adds to the general understanding of radiatively inefficient hot flows in accretion disks in X-ray binaries and active galactic nuclei, as it comprises a nonrelativistic limit at lower temperatures with a hard surface on the compact accretor (with significantly low or no magnetic field).

Acknowledgments

The authors thank M. Mendez and J. P. Lasota for useful discussions and/or comments on the manuscript. Ş.B. acknowledges a grant from the Scientific Research Projects Coordination Unit of Istanbul University through BAP Project No. 40017. This research is based on observations obtained with XMM-Newton, an ESA science mission with instruments and contributions directly funded by ESA Member States and NASA. This work has made use of data and software provided by the High Energy Astrophysics Science Archive Research Center (HEASARC) maintained by NASA/GSFC.

ORCID iDs

Şölen Balman https://orcid.org/0000-0001-6135-1144
Eric M. Schlegel https://orcid.org/0000-0002-4162-8190
Patrick Godon https://orcid.org/0000-0002-4806-5319
Jeremy J. Drake https://orcid.org/0000-0002-0210-2276

References

Aranzana, E., Scaringi, S., Körding, E., Dhillon, V. S., & Coppejans, D. L. 2018, MNRAS, 481, 2140
Arnaud, K. A. 1996, in ASP Conf. Ser. 101, Astronomical Data Analysis Software and Systems V, ed. G. H. Jacoby & J. Barnes (San Francisco, CA: ASP), 17
Bailey, J. 1979, MNRAS, 187, 645
Balman, Ş. 2009, AJ, 138, 50
Balman, S. 2012, MmSAI, 83, 585
Balman, S. 2014, in Proc. Frontier Research in Astrophysics (FRAPWS2014), ed. F. Giovannelli & L. Sabau-Graziati (Trieste: PoS), 9
Balman, S. 2015, AcPPP, 2, 116
Balman, Ş. 2019, AN, 340, 296
Balman, Ş. 2020, AdSpR, 66, 1097
Balman, Ş., Godon, P., Sion, E. M., et al. 2011, ApJ, 741, 84
Balman, Ş., & Revnivtsev, M. 2012, A&A, 546, A112
Balman, Ş., Schlegel, E. M., & Godon, P. 2022, ApJ, 932, 33
Baptista, R., Jablonski, F., Oliveira, E., et al. 2002, MNRAS, 335, L75
Bateson, F. M. 1978, MNRAS, 184, 567
Belloni, T. M., Motta, S. E., & Muñoz-Darias, T. 2011, BASI, 39, 409
Brown, G. V., Beiersdorfer, P., Chen, H., Chen, M. H., & Reed, K. J. 2001, ApJL, 557, L75
Bruch, A. 1996, A&A, 312, 97
Byckling, K., Osborne, J. P., Wheatley, P. J., et al. 2009, MNRAS, 399, 1576
Chen, G.-X., & Pradhan, A. K. 2005, arXiv:astro-ph/0510534
Collins, D. J., & Wheatley, P. J. 2010, MNRAS, 402, 1816
Cook, M. C., & Warner, B. 1984, MNRAS, 207, 705
Coppejans, D. L., & Knigge, C. 2020, NewAR, 89, 101540
Datta, S. R., Dhang, P., & Mishra, B. 2021, ApJ, 918, 87
de Avellar, M. G. B., Porth, O., Younsi, Z., & Rezzolla, L. 2018, MNRAS, 474, 3967
Del Santo, M., Belloni, T. M., Tomsick, J. A., et al. 2016, MNRAS, 456, 3585
den Herder, J. W., Brinkman, A. C., Kahn, S. M., et al. 2001, A&A, 365, L7
Díaz Trigo, M., & Boirin, L. 2016, AN, 337, 368
Dickey, J. M., & Lockman, F. J. 1990, ARA&A, 28, 215
Dobrotka, A., Ness, J.-U., & Bajčičáková, I. 2016, MNRAS, 460, 458
Dobrotka, A., Ness, J. U., Nucita, A. A., & Melicherčík, M. 2023, A&A, 674, A188
Dutta, A., Rana, V., Mukai, K., & de Oliveira, R. L. 2023, ApJ, 957, 33
Esin, A. A., McClintock, J. E., & Narayan, R. 1997, ApJ, 489, 865
Fender, R. P., Belloni, T. M., & Gallo, E. 2004, MNRAS, 355, 1105
Ferreira, J. 1997, A&A, 319, 340
Fertig, D., Mukai, K., Nelson, T., & Cannizzo, J. K. 2011, PASP, 123, 1054
Godon, P. 2019, ApJ, 870, 112
Godon, P., Regev, O., & Shaviv, G. 1995, MNRAS, 275, 1093
Godon, P., Sion, E. M., Balman, S. ¸, & Blair, W. P. 2017, ApJ, 846, 52
Güver, T., Uluyazı, C., Özkan, M. T., & Göğüs, E. 2006, MNRAS, 372, 450
Hameury, J. M., Knigge, C., Lasota, J. P., Hambsch, F. J., & James, R. 2020, A&A, 636, A1
Hameury, J. M., & Lasota, J. P. 2021, A&A, 650, A114
Hameury, J.-M., Lasota, J.-P., & Warner, B. 2000, A&A, 353, 244
Hamilton, R. T., Harrison, T. E., Tappert, C., & Howell, S. B. 2011, ApJ, 728, 16
Hertfelder, M., & Kley, W. 2015, A&A, 579, A54
Hertfelder, M., & Kley, W. 2017, A&A, 605, A24
Hessman, F. V. 1999, ApJ, 510, 867
Horne, K., Marsh, T. R., Cheng, F. H., Hubeny, I., & Lanz, T. 1994, ApJ, 426, 294
Hubeny, I., & Long, K. S. 2021, MNRAS, 503, 5534
Ishida, M., Okada, S., Hayashi, T., et al. 2009, PASJ, 61, S77
Jansen, F., Lumb, D., Altieri, B., et al. 2001, A&A, 365, L1
Kimura, M., Kashiyama, K., Shigeyama, T., et al. 2023, ApJ, 951, 124
Kimura, M., Yamada, S., Nakaniwa, N., et al. 2021, PASJ, 73, 1262
Knigge, C., Baraffe, I., & Patterson, J. 2011, ApJS, 194, 28
Knigge, C., Long, K. S., Wade, R. A., et al. 1998, ApJ, 499, 414
Körding, E., Rupen, M., Knigge, C., et al. 2008, Sci, 320, 1318
Kuulkers, E., Norton, A., Schwope, A., & Warner, B. 2006, X-rays from Cataclysmic Variables, Vol. 39 (Cambridge: Cambridge Univ. Press), 421
La Dous, C. 1989, MNRAS, 238, 935
Lasota, J.-P. 2001, NewAR, 45, 449
Lasota, J. P. 2004, RMxAA, 20, 124
Lasota, J. P. 2008, NewAR, 51, 752
Liedahl, D. A. 1999, in The X-Ray Spectral Properties of Photoionized Plasma and Transient Plasmas, ed. J. van Paradijs & J. A. M. Bleeker, Vol. 520 (Berlin: Springer), 189
Liedahl, D. A., Osterheld, A. L., & Goldstein, W. H. 1995, ApJL, 438, L115
Linnell, A. P., Godon, P., Hubeny, I., Sion, E. M., & Szkody, P. 2010, ApJ, 719, 271
Long, K. S., Mauche, C. W., Raymond, J. C., Szkody, P., & Mattei, J. A. 1996, ApJ, 469, 841
Lubow, S. H. 1989, ApJ, 340, 1064
Lynden-Bell, D., & Pringle, J. E. 1974, MNRAS, 168, 603

Marcel, G., Cangemi, F., Rodriguez, J., et al. 2020, A&A, 640, A18
Marcel, G., Ferreira, J., Clavel, M., et al. 2019, A&A, 626, A115
Marsh, T. R. 1986, PhD Thesis, Univ. Cambridge
Mason, K. O., Breeveld, A., Much, R., et al. 2001, A&A, 365, L36
Mauche, C. W. 2004, ApJ, 610, 422
Mauche, C. W., & Raymond, J. C. 2000, ApJ, 541, 924
Mauche, C. W., Raymond, J. C., & Mattei, J. A. 1995, ApJ, 446, 842
McGowan, K. E., Priedhorsky, W. C., & Trudolyubov, S. P. 2004, ApJ, 601, 1100
Meyer, F., & Meyer-Hofmeister, E. 1994, A&A, 288, 175
Miller, J. M., Raymond, J., Reynolds, C. S., et al. 2008, ApJ, 680, 1359
Mukai, K. 2017, PASP, 129, 062001
Narayan, R., & Popham, R. 1993, Natur, 362, 820
Narayan, R., & Yi, I. 1994, ApJL, 428, L13
Neilsen, J., & Lee, J. C. 2009, Natur, 458, 481
Nishino, Y., Kimura, M., Sako, S., et al. 2022, PASJ, 74, L17
Nixon, C. J., & Pringle, J. E. 2019, A&A, 628, A121
Nucita, A. A., Kuulkers, E., Maiolo, B. M. T., et al. 2011, A&A, 536, A75
Okada, S., Nakamura, R., & Ishida, M. 2008, ApJ, 680, 695
Osaki, Y. 1996, PASP, 108, 39
Pandel, D., Córdova, F. A., Mason, K. O., & Priedhorsky, W. C. 2005, ApJ, 626, 396
Parthasarathy, V., Kluźniak, W., & Čemeljić, M. 2017, MNRAS, 470, L34
Patterson, J., & Raymond, J. C. 1985, ApJ, 292, 535
Ponti, G., Fender, R. P., Begelman, M. C., et al. 2012, MNRAS, 422, L11
Popham, R. 1999, MNRAS, 308, 979
Popham, R., & Narayan, R. 1995, ApJ, 442, 337
Porquet, D., & Dubau, J. 2000, A&AS, 143, 495
Porter, R. L., & Ferland, G. J. 2007, ApJ, 664, 586
Pratt, G. W., Hassall, B. J. M., Naylor, T., Wood, J. H., & Patterson, J. 1999, MNRAS, 309, 847
Puebla, R. E., Diaz, M. P., & Hubeny, I. 2007, AJ, 134, 1923
Rana, V. R., Singh, K. P., Schlegel, E. M., & Barrett, P. E. 2006, ApJ, 642, 1042
Rayne, M. W., & Whelan, J. A. J. 1981, MNRAS, 196, 73
Remillard, R. A., & McClintock, J. E. 2006, ARA&A, 44, 49
Rezzolla, L., Yoshida, S., & Zanotti, O. 2003, MNRAS, 344, 978
Robinson, E. L., Wood, J. H., Bless, R. C., et al. 1995, ApJ, 443, 295
Robinson, E. L., Wood, J. H., & Wade, R. A. 1999, ApJ, 514, 952
Scaringi, S. 2014, MNRAS, 438, 1233
Schlegel, E. M., Shipley, H. V., Rana, V. R., Barrett, P. E., & Singh, K. P. 2014, ApJ, 797, 38
Schreiber, M. R., Hameury, J. M., & Lasota, J. P. 2003, A&A, 410, 239
Shakura, N. I., & Sunyaev, R. A. 1973, A&A, 500, 33
Silver, E., Schnopper, H., Bandler, S., et al. 2000, ApJ, 541, 495
Singh, K. P., White, N. E., & Drake, S. A. 1996, ApJ, 456, 766
Smak, J. 1979, AcA, 29, 309
Smak, J. 2007, AcA, 57, 87
Smak, J. 2012, AcA, 62, 213
Smith, R. K., & Hughes, J. P. 2010, ApJ, 718, 583
Stehle, R., & King, A. R. 1999, MNRAS, 304, 698
Strüder, L., Briel, U., Dennerl, K., et al. 2001, A&A, 365, L18
Szkody, P., Nishikida, K., Raymond, J. C., et al. 2002, ApJ, 574, 942
Takeo, M., Hayashi, T., Ishida, M., Nakaniwa, N., & Maeda, Y. 2021, PASJ, 73, 143
Turner, M. J. L., Abbey, A., Arnaud, M., et al. 2001, A&A, 365, L27
van Teeseling, A. 1997, A&A, 319, L25
Wada, Q., Tsujimoto, M., Ebisawa, K., & Hayashi, T. 2017, PASJ, 69, 10
Wade, R. A., & Horne, K. 1988, ApJ, 324, 411
Warner, B. 1974, MNRAS, 168, 235
Warner, B. 1995, Cataclysmic Variable Stars, Vol. 28 (Cambridge: Cambridge Univ. Press),
Wheatley, P. J., Mauche, C. W., & Mattei, J. A. 2003, MNRAS, 345, 49
Willingale, R., Starling, R. L. C., Beardmore, A. P., Tanvir, N. R., & O'Brien, P. T. 2013, MNRAS, 431, 394
Wilms, J., Allen, A., & McCray, R. 2000, ApJ, 542, 914
Wood, J., Horne, K., Berriman, G., et al. 1986, MNRAS, 219, 629
Wood, J. H. 1990, MNRAS, 243, 219
Wood, J. H., & Horne, K. 1990, MNRAS, 242, 606
Yuan, F., & Narayan, R. 2014, ARA&A, 52, 529